

Article

Multi-Objective Optimization of Back-to-Back Starting for Pumped Storage Plants under Low Water Head Conditions Based on the Refined Model

Chen Feng ¹, Guilin Li ^{1,*}, Yuan Zheng ¹, Daqing Zhou ¹  and Zijun Mai ²¹ College of Energy and Electrical Engineering, Hohai University, Nanjing 211100, China² Department of Rural Water Management, Nanjing Hydraulic Research Institute, Nanjing 210029, China

* Correspondence: windycity@hhu.edu.cn; Tel.: +86-150-7199-5381

Abstract: Pumped storage plants (PSP) must switch frequently between various working conditions. Moreover, PSPs can fall easily into an S-shaped zone under low water head conditions, especially during back-to-back starting (BTBS), which reduces the stability and safety of unit operation. In this paper, a nonlinear PSP model for BTBS is established by combining an electrical subsystem with a refined hydraulic-mechanical subsystem. The influences of the hydraulic, mechanical, and electrical factors on the BTBS process are investigated quantitatively. Choosing the speed overshoot and speed stable time as the optimization objectives, and considering a variety of constraints, the multi-objective particle swarm optimization (MOPSO) algorithm is introduced to study and optimize two typical startup strategies. The results show that: (1) The parameters of a hydraulic-mechanical-electrical system have a significant impact on BTBS process, and the most unfavorable working condition corresponds to the lowest water head; (2) In the control schemes, a novel constant excitation voltage strategy is proposed based on the multi-objective optimization scheme. Compared with the constant excitation current strategy or single-objective, the optimization strategy proposed can considerably improve the speed overshoot and the speed stable time by at least 68.27% and 3.22% under the worst working conditions. (3) It is further verified that the problem of trapping in the S-shaped region under various working conditions may be avoided by the obtained optimal control scheme. The results give prominence to the effectiveness of the proposed optimization strategy for maintaining the safety and stabilization of PSP operation.

Keywords: pumped storage plant; back-to-back starting; low water head condition; constant excitation voltage; multi-objective optimization; optimal control scheme



Citation: Feng, C.; Li, G.; Zheng, Y.; Zhou, D.; Mai, Z. Multi-Objective Optimization of Back-to-Back Starting for Pumped Storage Plants under Low Water Head Conditions Based on the Refined Model. *Sustainability* **2022**, *14*, 10289. <https://doi.org/10.3390/su141610289>

Academic Editor: Dino Musmarra

Received: 19 July 2022

Accepted: 15 August 2022

Published: 18 August 2022

Publisher's Note: MDPI stays neutral with regard to jurisdictional claims in published maps and institutional affiliations.



Copyright: © 2022 by the authors. Licensee MDPI, Basel, Switzerland. This article is an open access article distributed under the terms and conditions of the Creative Commons Attribution (CC BY) license (<https://creativecommons.org/licenses/by/4.0/>).

1. Introduction

In order to cope with climate change, many renewable energy sources have been developed, such as tidal, wind, solar, and hydro energies [1]. As unstable renewable energy is connected to the grid in large quantities and the load demand is diversified, the power grid's supply and demand fluctuation is becoming more serious [2,3]. As an essential energy storage technology, a pumped storage plant (PSP) can effectively adjust the impact of unstable energy on the power system and enhance the consumption capacity of the power grid for unstable energy such as solar energy and wind power [4,5]. However, during the large fluctuation transition process of the pumped storage unit (PSU), due to the influence of the S-shaped curve of the pump turbine, the water hammer effect in the penstock of the diversion system causes an effect similar to the rapid closing of guide vanes, and the inflow decreases rapidly, resulting in the sharp rise of water pressure and speed, threatening the structural safety of unit and diversion pipelines [6,7]. The above operation characteristics and various potential operation accidents not only seriously endanger the safe and stable operation of PSPs, but also affect the safety and stability of the power supplies.

At present, the conventional startup mode of large PSPs at home and abroad is mainly via a static frequency converter starting and BTBS as standby [8–10]. During variable frequency starting, it is necessary to absorb electric energy from the power grid. If the power grid or the frequency converter fails, the unit cannot be started in this way, but the BTBS mode can meet the requirements well. Therefore, the experience and technology of BTBS should be explored in the context of building a resilient power grid. Among the numerous startup conditions of the PSU, the BTBS mode is the most complicated, requiring the mutual cooperation of monitoring, speed regulation, excitation, protection, and other systems of the two units, which presents an enormous challenge to the stable operation of PSPs. However, this issue has not been fully addressed until now. Previous studies have mainly focused on the transient electrical characteristics and electromechanical variation law. Relevant research findings are summarized as follows:

For BTBS modelling, previous studies focus on the electrical perspective by greatly simplifying the hydraulic and mechanical systems. The functions offered by turbine manufacturers and obtained by model tests, which are used to describe the dynamic behaviors among the mechanical torque, gate valve opening (GVO), and speed, have been widely adopted [11,12]. However, these models are mostly oversimplified based on strong assumptions in reflecting the coupling characteristics of the hydraulic-mechanical-electrical subsystems of a PSP under various working conditions, especially the S-shaped characteristics under low head conditions. Therefore, a nonlinear model with a detailed hydraulic-mechanical system, i.e., the logarithmic curve projection (LCP) method for pump turbine [13], and the method of characteristics (MOC) for conduit systems [14], has been adopted to improve the accuracy of the BTBS transient processes simulation in this work, which can overcome the shortcomings of the above-simplified models.

For analysis of influencing factors, Konidaris [12] systematically discussed the main parameters' impact on the performance of the BTBS based on the physical laws behind the transient process. Osburn and Atwater [15] described the design and testing of a BTBS system. The feasibility of this kind of startup is analyzed theoretically. Guidance was developed in order to correctly select the main parameters for a successful start [16]. By means of simulating the transient starting performance for a PSU, alternative designs and their effects on the startup ability of the PSU for reliable improvement of the starting system were studied [17]. Proposals were offered to achieve safe and reliable fault clearance on the basis of the fault characteristics and actual deexcitation test results of the PSP [18].

For control optimization, there are many applications of the MOPSO algorithm in energy systems; A. Beiranvand applied the MOPSO algorithm in the optimization analysis of thermal power generation [19], and M. Ghazvini proposed the Coupled Multi-Objective Evolutionary Approaches [20]. There are also multi-objective optimization cases in the field of materials and chemicals [21,22], which give some inspiration to this paper. However, the BTBS model is more complicated. There exists no report on the optimization of the BTBS control scheme, and only some research on the startup strategy of PSPs under turbine conditions has been involved. Xu et al. [23] studied the optimal control for the turbine startup process of PSPs under low head conditions. There are hydraulic, mechanical, and electrical interferences between two units, and more control factors must be taken into account during the BTBS process. Moreover, BTBS generally happens during the low power consumption period, and the upper-reservoir water storage has been exhausted during the peak power consumption period. Thus, the PSU can more easily be under low water head conditions and fall into the S-shaped zone.

Through reviews of relevant works, it was found that too little work has been devoted to BTBS in the previous research, which mainly focused on the BTBS workflow or the influence of electrical factors on the transient process of BTBS. Many other factors, such as effects from the S-shaped characteristics, are likely to affect the transient processes of BTBS and have not been studied. In addition, to our best knowledge, the control scheme optimization strategy for BTBS has not been proposed in previous works.

Accordingly, in this paper, the effect mechanisms of the hydraulic-mechanical-electrical coupling factors on BTBS are investigated, and the optimization strategy for BTBS control at low water head conditions is proposed. A nonlinear model for PSP by incorporating an electrical subsystem with a refined hydraulic-mechanical subsystem is established to conduct the study, and the effects of the electrical and hydraulic-mechanical subsystems on the process of BTBS are quantitatively investigated subsequently. Moreover, on the basis of the analysis of the influencing factors, a novel multiobjective optimization scheme for the BTBS control strategy is proposed. The innovations of this paper are as follows.

- (1) It is the first to establish a nonlinear PSP model combining the electrical subsystem with the fine hydraulic and mechanical subsystems for BTBS;
- (2) The effects of the hydraulic-mechanical-electrical parameters on the BTBS are comprehensively investigated on the basis of the model mentioned above;
- (3) An innovative multi-objective optimization scheme is proposed for the control strategy of BTBS at low water head conditions for the first time, which is proven to be suitable for a variety of working conditions.

The remainder of the paper proceeds as follows: The nonlinear model of a PSP with a refined hydraulic-mechanical subsystem is constructed and validated in Section 2. In Section 3, the effects of the hydraulic-mechanical-electrical parameters on the BTBS processes are then studied. In Section 4, an innovative multi-objective optimization scheme for BTBS in the condition of low head is proposed on the basis of the analysis above. In Section 5, a case study is conducted and the optimization result is also authenticated in other working conditions. In Section 6, the conclusions of these analyses are brought forth. Figure 1 presents the flowchart of this research.

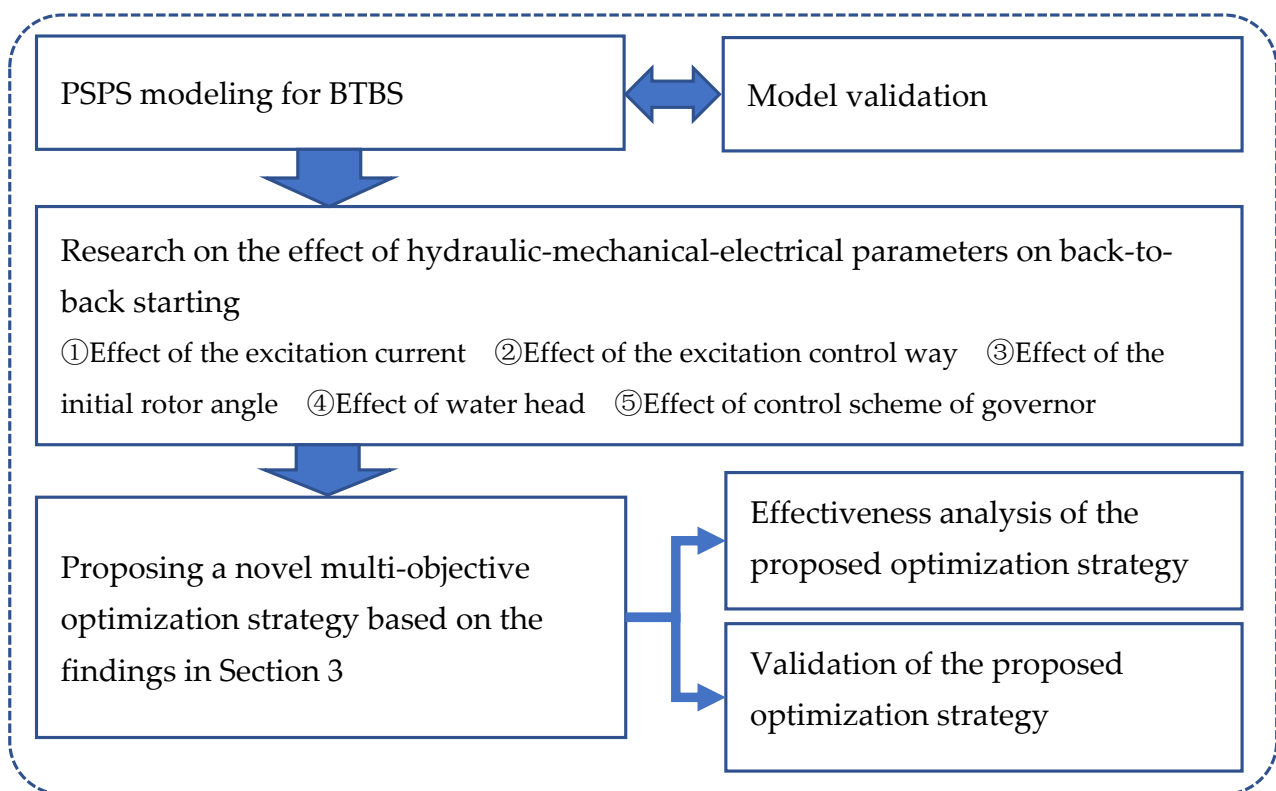


Figure 1. A flowchart of the research in this paper.

2. Refined Modelling of a Pumped Storage Plant for Back-to-Back Starting

The BTBS mode is also called synchronous starting mode, which uses one PSU as a generator to provide the current with increasing frequency. The other PSU to be started is

used as a motor, and the current with variable-frequency output by the former is used to accelerate to the rated speed synchronously. The BTBS is affected by the coupling factors of the hydraulic-mechanical and electrical systems. The basic form of BTBS is shown in Figure 2.

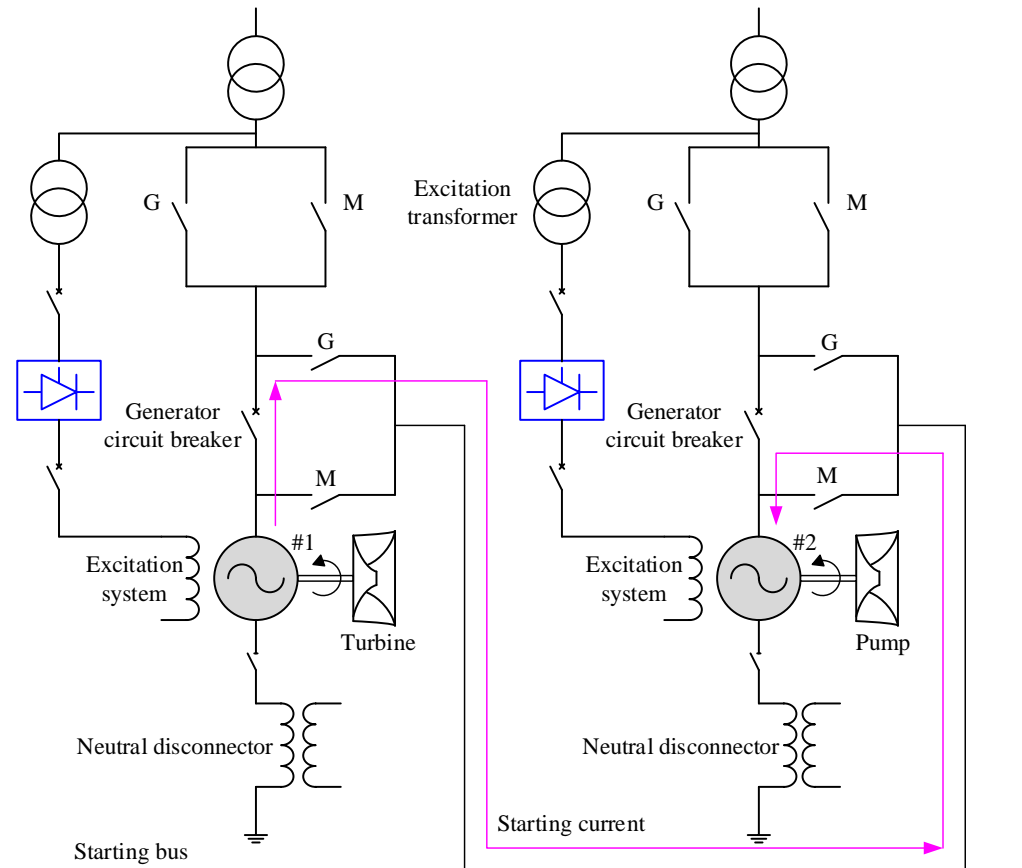


Figure 2. The basic form of back-to-back starting.

2.1. The Hydraulic-Mechanical Subsystem

(1) Conduit System

On the basis of hydromechanical theory, the momentum and continuity equations, which describe the unsteady pressure and flow in penstocks, can be formulated as follows [24]:

$$\frac{\partial Q}{\partial t} + gA \frac{\partial H}{\partial x} + \frac{f}{2dA} Q|Q| = 0 \quad (1)$$

$$a^2 \frac{\partial Q}{\partial x} + gA \frac{\partial H}{\partial t} = 0 \quad (2)$$

The details of all variable symbols in the study are presented in the Nomenclature. The MOC method is used to solve the above equations, considering the elasticity of the water hammer in the penstocks [25].

(2) The Pump turbine Model

As the key equipment of energy conversion, it is crucial to model the pump turbine accurately. At present, the characteristic curves have been widely adopted in nonlinear modelling for pump turbines provided by manufacturers, as shown in Figure 3. The nonlinear model can be described by (3) and (4):

$$\begin{cases} M_{11} = f_M(Y, N_{11}) \\ Q_{11} = f_Q(Y, N_{11}) \end{cases} \quad (3)$$

$$\begin{cases} M_t = M_{11} D^3 H_t \\ Q_t = Q_{11} D^2 \sqrt{H_t} \\ N = N_{11} \sqrt{H_t} / D \end{cases} \quad (4)$$

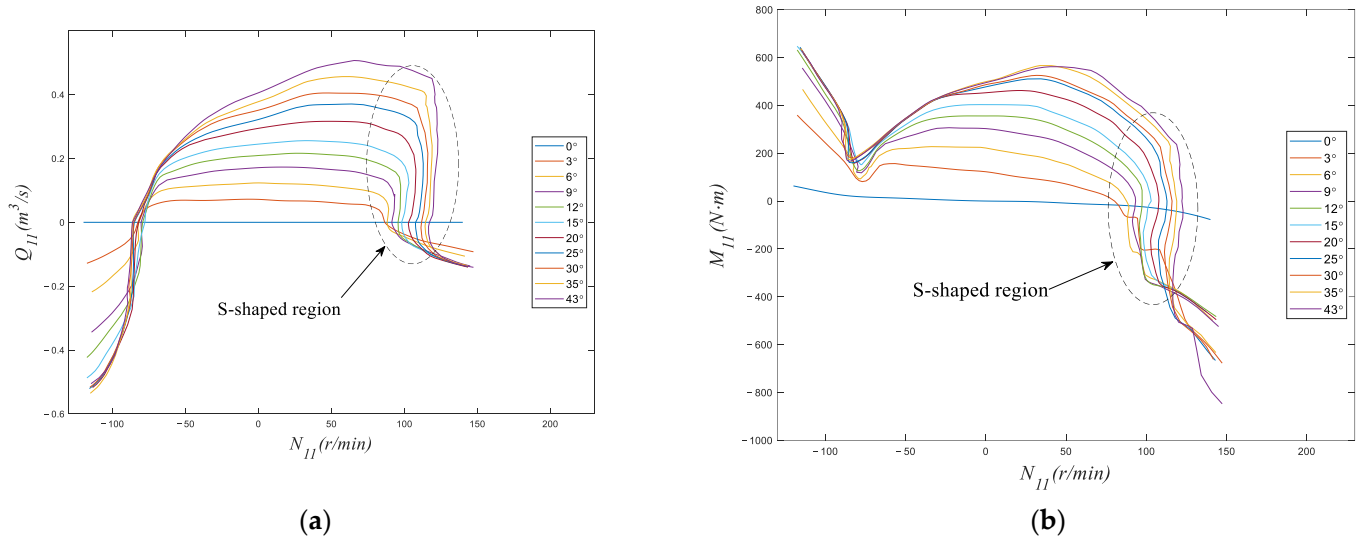


Figure 3. Characteristic curves of a pump turbine. (a) Flow characteristic curve. (b) Moment characteristic curve.

As shown in Figure 3, the S-shaped area raises obstacles for the pump turbine modelling, which presents a multivalued characteristic. The Logarithmic-Curve-Projection (LCP) method [13] is proposed to convert the unit speed N_{11} in the way of logarithmic projection so as to overcome the difficulty. The equation is as follows:

$$\begin{cases} X = n_{11} / e^{q_{11}} \\ n_{11} = N_{11} / N_{11r} \\ q_{11} = Q_{11} / Q_{11r} \end{cases} \quad (5)$$

The results obtained by means of the LCP method are shown in Figure 4; the LCP curves reflect the change rule of Q_{11} and M_{11} with abscissa X . It immensely reduces the complexity of the calculation procedure problems whether compared with the Suter or improved Suter methods [26].

Thereafter, in a given moment, the unit moment and the unit flow are computed using interpolation in accordance with the LPC curves.

(3) The Turbine Governor System

The governor of the PSP is comprised of a controller and servomechanism. As the actuator of the governor, the servomechanism uses the output signal of the PID controller to drive the guide vanes. Considering the main nonlinear factors (dead zone, saturation, and output limiting), the whole model of the governor is shown in Figure 5.

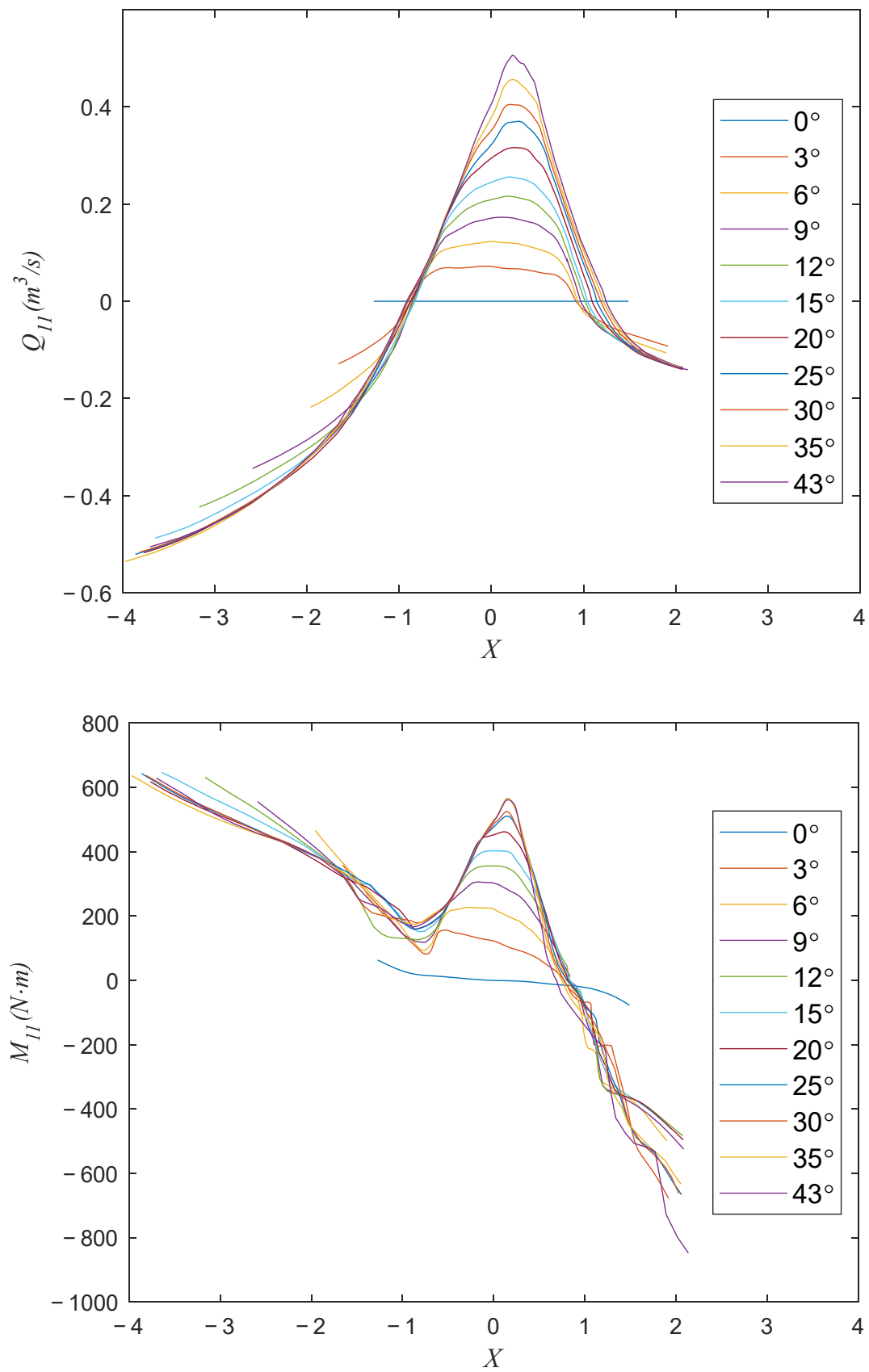


Figure 4. Logarithmic-Curve-Projection of the characteristic curves.

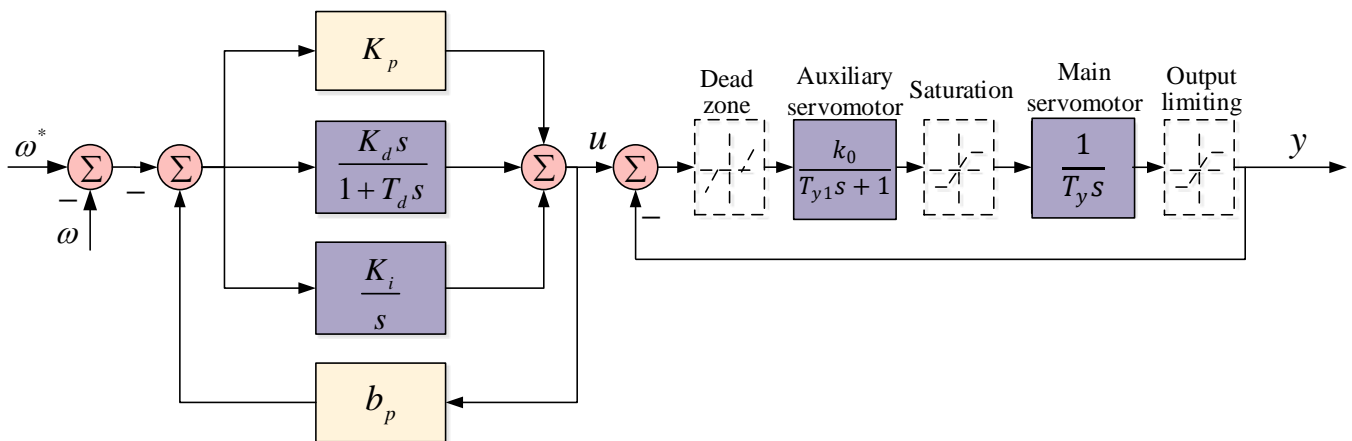


Figure 5. Block diagram of the governor system with nonlinear mechanical components.

2.2. The Electrical Subsystem

(1) Synchronous Machine

Since it is very difficult to gain an accurate value of the original parameters of the synchronous machine through analysis and calculation, 18 original parameters of a synchronous machine are usually converted into 11 machine parameters composed of steady-state, transient, and sub-transient parameters in engineering, which can be obtained directly through experiments. The mathematical model of a synchronous machine expressed by 11 machine parameters includes voltage balance equations of stator winding (8), excitation equations of stator winding (9), voltage balance equations of rotor winding (10), and a rotor motion Equation (11) [27].

$$\begin{cases} v_d = \dot{\varphi}_d - \omega \dot{\varphi}_q - R_a i_d \\ v_q = \dot{\varphi}_q + \omega \dot{\varphi}_d - R_a i_q \end{cases} \quad (6)$$

$$\begin{cases} \varphi_d = E_q'' - X_d'' i_d \\ \varphi_q = -E_d'' - X_q'' i_q \end{cases} \quad (7)$$

$$\begin{cases} T'_{d0} \dot{E}_q' = -\frac{X_d - X_d''}{X_d' - X_d''} E_q' + \frac{X_d - X_d''}{X_d' - X_d''} E_q'' + E_{fd} \\ T''_{d0} \dot{E}_q'' = E_q' - E_q'' - (X_d' - X_d'') i_d \\ T'_{q0} \dot{E}_d' = -\frac{X_q - X_q''}{X_q' - X_q''} E_d' + \frac{X_q - X_q''}{X_q' - X_q''} E_d'' \\ T''_{q0} \dot{E}_d'' = E_d' - E_d'' + (X_q' - X_q'') i_q \end{cases} \quad (8)$$

$$\begin{cases} \dot{\delta} = (\omega - 1)\omega_0 \\ T_j \dot{\omega} = M_t - M_e \end{cases} \quad (9)$$

(2) The Excitation System

A DC exciter is adopted, as shown in Figure 6 [28]. The primary elements of the excitation system block are the lead-lag compensator, main regulator, exciter, and damping block.

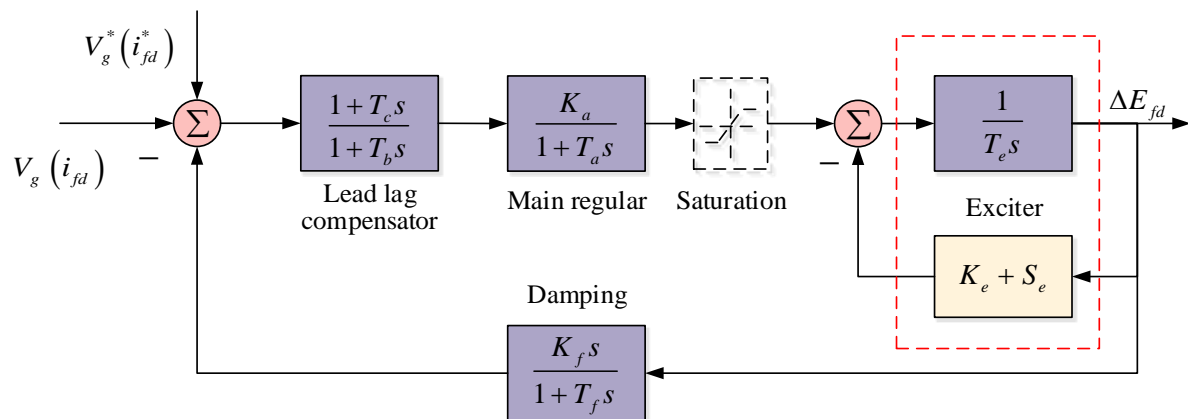


Figure 6. Block diagram of the excitation system.

2.3. Model Validation with On-Site Measurement

The proposed PSP model is validated by a case study in this subsection. In previous studies, in many cases the electrical subsystem model has been validated by measurement [29]. Therefore, the goal of this paper is to use the model to prove the hydraulic-mechanical subsystem.

The research data in this section are from a large PSP in Hubei Province of China, and the topology of its regulation system is shown in Figure 7. The parameters of the pump turbine and the generator and motor of the PSU are shown in Table A1, and the characteristic curves of the pump turbine are shown in Figure 3. The pipeline parameters of the diversion system that can be used for modelling after processing are shown in Table A2. The dimensional parameters of the surge chamber are shown in Table A3. In addition, the basic parameters of each module of the regulation system are shown in Table A4.

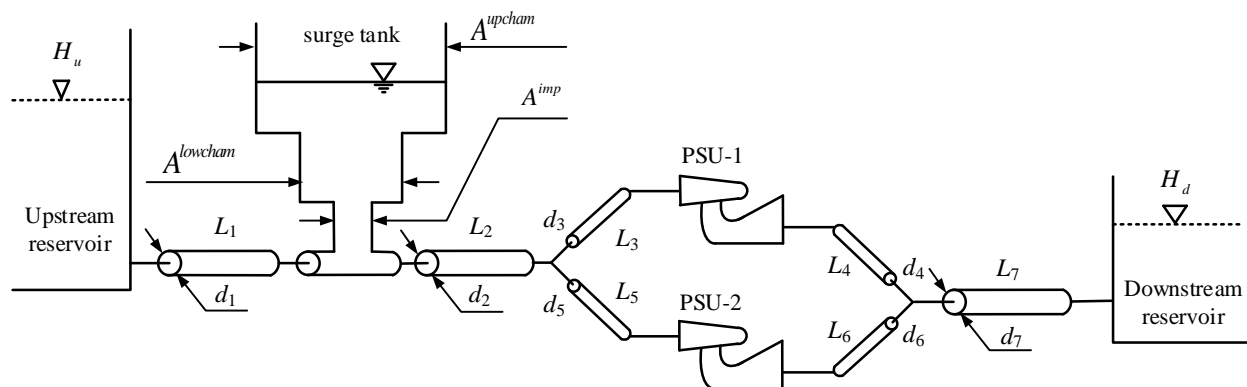


Figure 7. Layout diagram of the considered PSP.

In this case study, PSU-2 is offline when PSU-1 begins a single-unit load rejection. The water level of the upper reservoir is 306.98 m, and the downstream reservoir is 96.11 m, so the gross head is 210 m. When the PSU-1 operates normally with 300 MW load, the load is suddenly rejected. The guide vane is normally closed in 30 s. The variation waveform of various parameters in the simulation test is shown in Figure 8. Through analysis of the graph, the characteristic values of each parameter change are extracted and compared with the results of field measurements. Table 1 shows the comparison results.

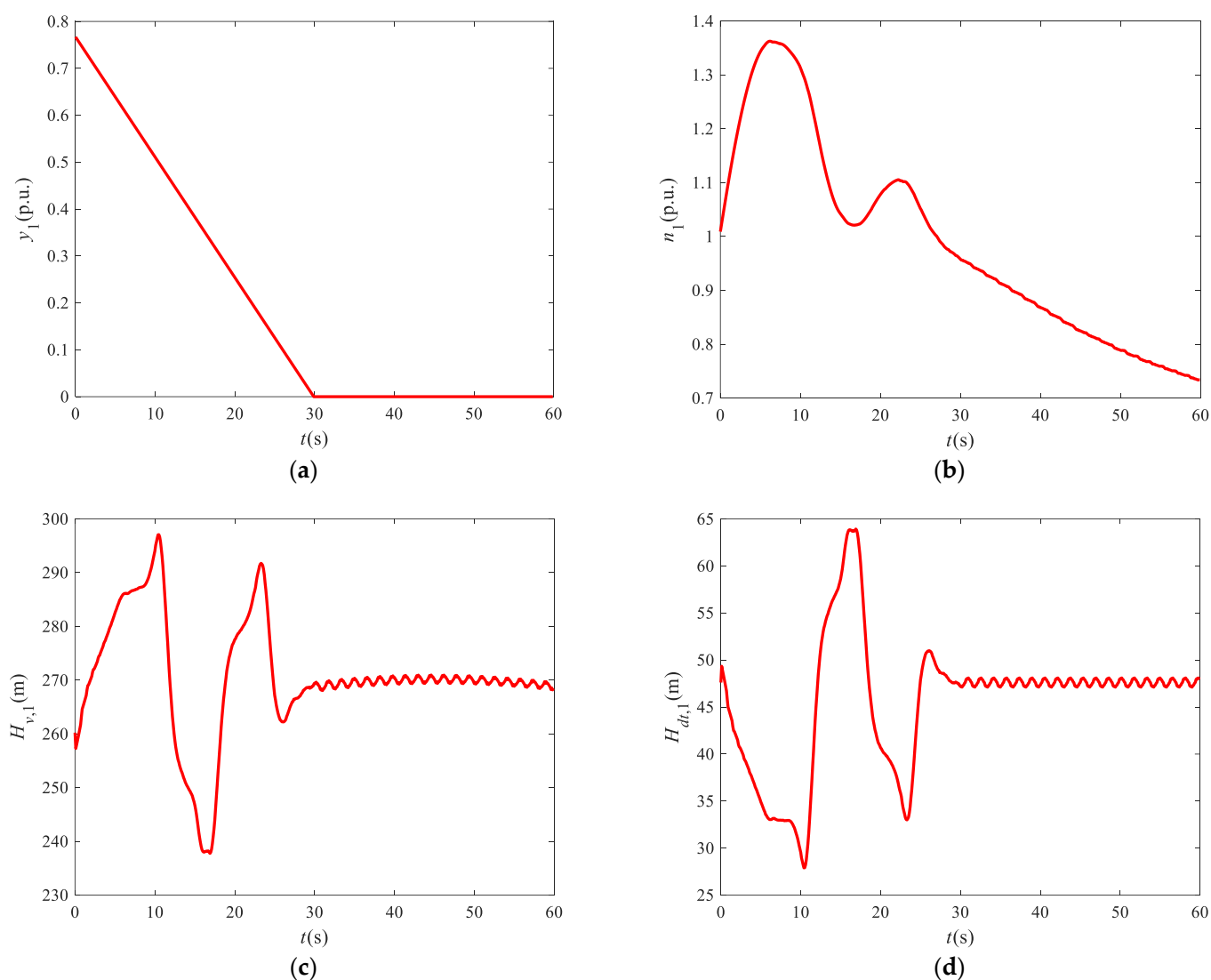


Figure 8. Simulation results of PSU-1 during a single-unit load rejection. (a) Guide vane opening. (b) Rotational speed. (c) Volute water pressure. (d) Draft tube water pressure.

Table 1. Full load rejection results of PSU-1 compared to on-site measurements.

Unit Number	Category	Maximum Pressure at Measuring Point of Volute Inlet	Minimum Water Pressure at MEASURING Point of Draft Tube	Maximum Speed
1#	Measurement	299.32 m	26.6 m	140%
	Refined model	297.05 m	27.9 m	136%
	Absolute error	−2.27 m	1.3 m	−4%
	Relative error	−0.75%	4.88%	2.85%

As revealed in Figure 8 and Table 1, the calculation results of the full load rejection transition process achieve consensus results with the on-site measurements, which effectively verifies the accuracy of the PSP mathematical model constructed in this paper.

3. Analysis of Factors Affecting Back-to-Back Starting

3.1. Excitation Current

The excitation system of the two units adopts separate excitation sources (grid-side power supply or auxiliary power supply), and the closed-loop control modes of the constant

excitation current (CEC) are adopted for the two units. After the speeds of the two units are synchronously accelerated to 90% of the rated value, the excitation control modes are changed to the closed-loop working modes of the constant terminal voltage. Figure 9 is an example of successful BTBS (given excitation current $i_g^* = 1.2, i_m^* = 0.6$), while Figure 10 is an example of a failed start due to improper matching of excitation current (given that excitation current $i_g^* = 0.8, i_m^* = 0.5$).

To explore the impact of given excitation current (i_g^*, i_m^*) on the BTBS process, BTBS under different excitation currents (i_g^*, i_m^*) are simulated, as may be observed in Figure 11. The range of i_{fd}^* is [0, 2], the default values are kept for other parameters of the PSP.

In Figure 11, The blue circle within the green area means that the BTBS is successful when the excitation current is (i_m^*, i_g^*). It shows that the BTBS results are altered by the given excitation current. The excitation current of the generator and motor must maintain an appropriate proportion to ensure successful BTBS. In particular, the proportion is affected by the characteristics of the units, and the requirements of the excitation current for the units are also different.

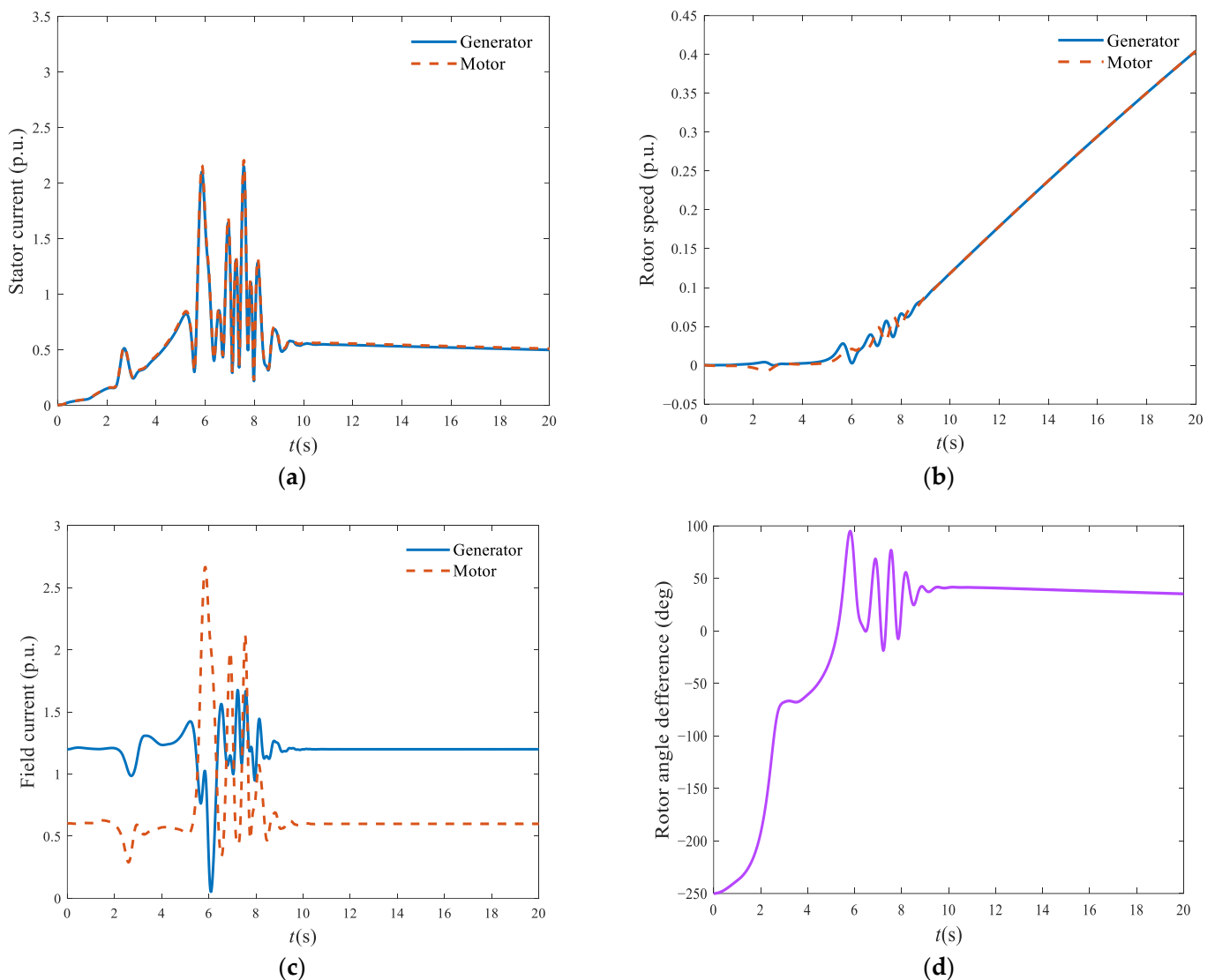


Figure 9. Successful BTBS of constant excitation current $i_{fd}^{g*} = 1.2, i_{fd}^{m*} = 0.6$. (a) Stator's current; (b) Rotor speed; (c) Field current; (d) Rotor angle difference.

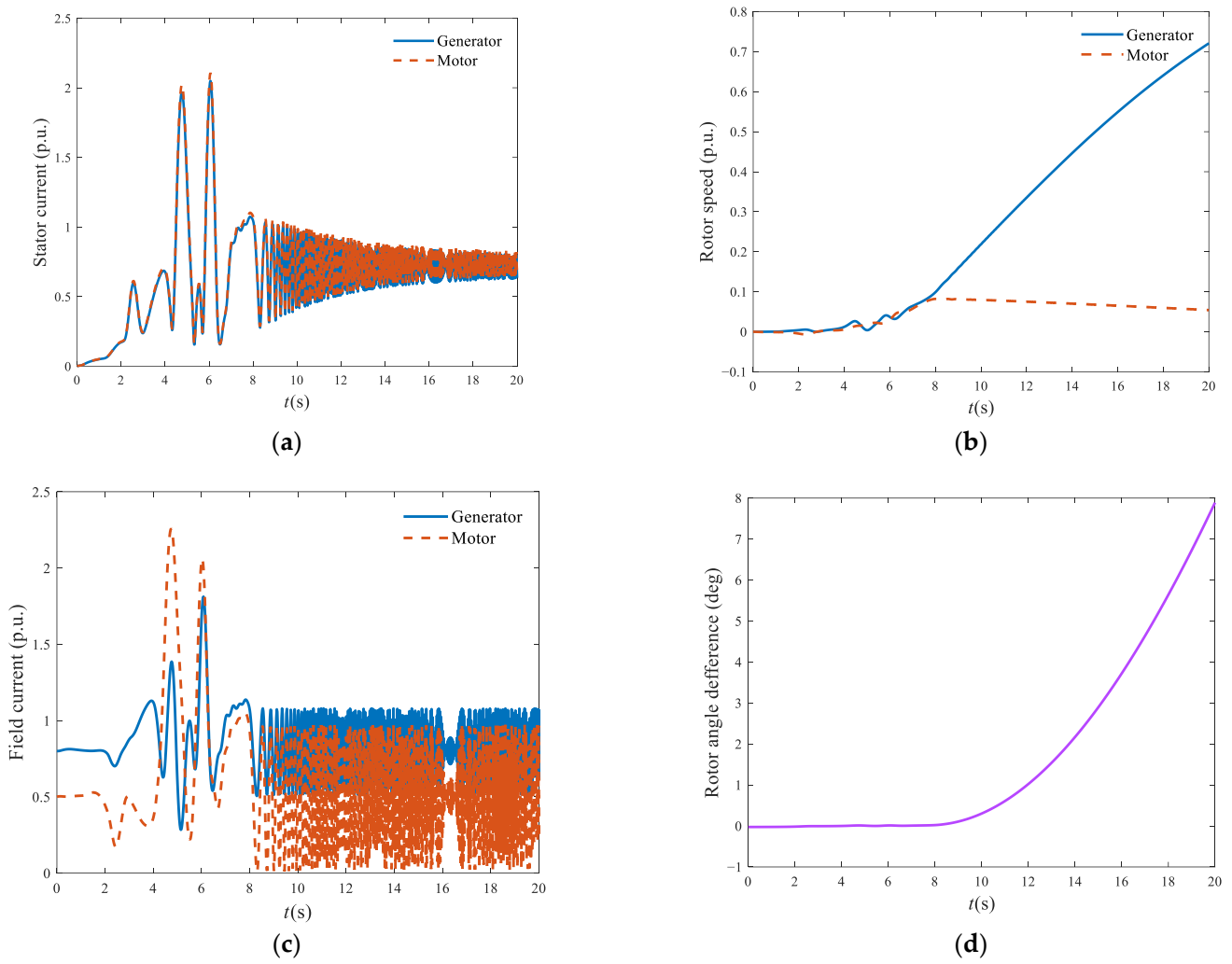


Figure 10. Unsuccessful BTBS of constant excitation current $i_{fd}^{g*} = 0.8, i_{fd}^{m*} = 0.5$. (a) Stator’s current; (b) Rotor speed; (c) Field current; (d) Rotor angle difference.

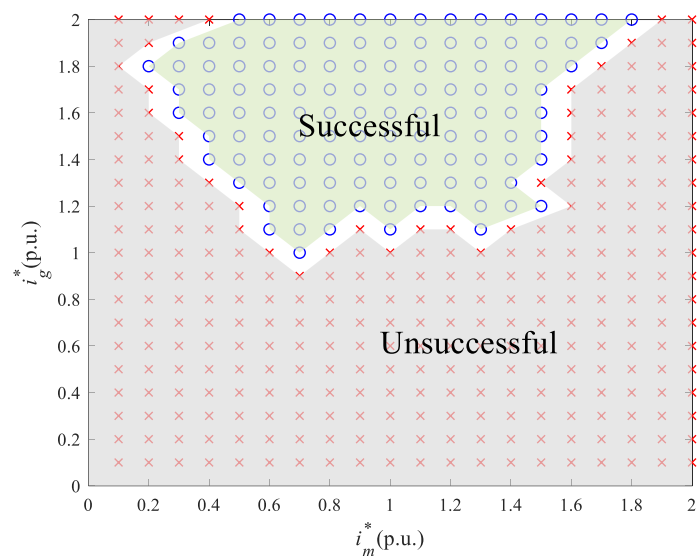


Figure 11. The influence of the given excitation current on the BTBS process.

3.2. Control Way of the Excitation System

There are usually four control modes of an excitation system: constant terminal voltage regulation, constant excitation current regulation, constant reactive power regulation, and constant power factor regulation [30]. However, in the BTBS process of a large PSU, the excitation mode is usually constant excitation current regulation or constant terminal voltage regulation.

One innovation of this paper is the discovery that the closed-loop working mode of constant excitation voltage (CEV) (Note: not constant terminal voltage) can also realize BTBS. Two control modes are simulated and compared. For the convenience of comparison, only the oscillation stages before the two machines run into synchronous acceleration are presented. The simulation results of BTBS with CEC ($i_g^* = 1.4, i_m^* = 1.2$) are shown in Figure 12. Figure 13 shows the simulation results of BTBS with CEV ($V_g^* = 1.4, V_m^* = 1.2$).

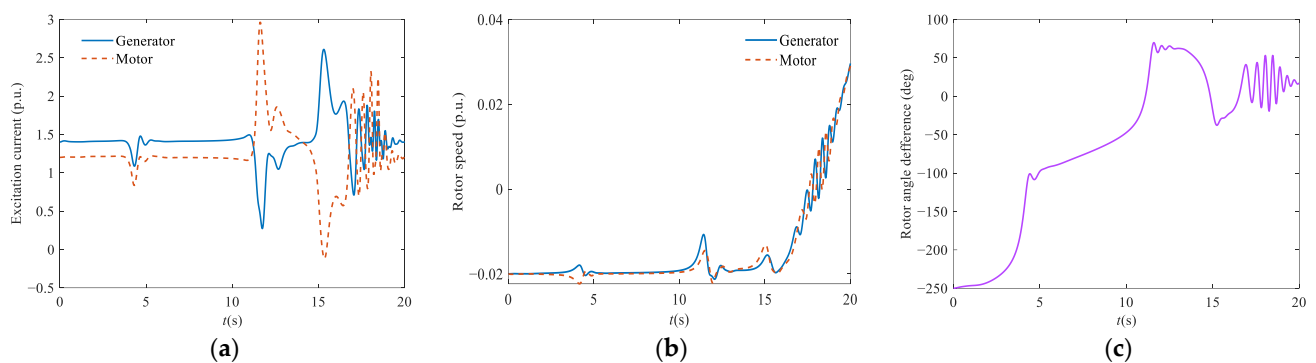


Figure 12. Simulation results of BTBS with CEC. (a) Excitation current; (b) Rotor speed; (c) Rotor angle difference.

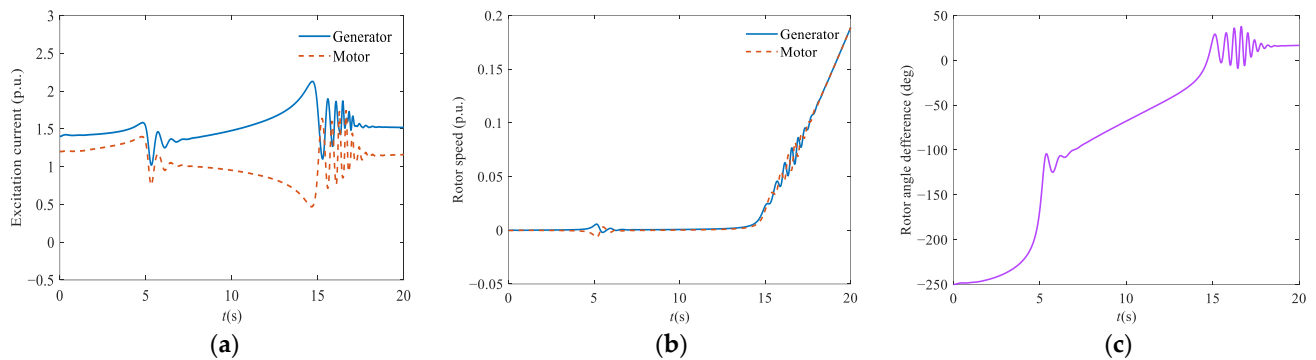


Figure 13. Simulation results of BTBS with CEV. (a) Excitation current; (b) Rotor speed; (c) Rotor angle difference.

By studying Figures 12 and 13, it is revealed that under the same initial conditions, the oscillation in the starting process of CEC is much larger than in that of CEV. The above physical process shows that there must be an oscillation process when the two machines enter the oscillation stage before synchronous acceleration. The rotor circuit passively plays a specific damping role in this oscillation process, and the excitation current will oscillate accordingly. If the CEC closed-loop mode is adopted, the excitation current of the two machines will be forced to remain constant, which will weaken the damping effect of the rotor circuit. When the closed-loop mode of CEV is adopted, the excitation current of the two machines is allowed to oscillate passively to a certain extent, which is equivalent to increasing the damping of the rotor circuit. In this way, the excitation circuit should adopt the closed-loop mode of CEV.

3.3. Initial Difference between Rotor Positions

Due to the randomness of the initial difference between rotor angles of two units, there must be an adjustment from the initial angle difference to the target angle difference, which begins after the water pump is started. Table 2 shows the BTBS results of the two machines under different initial angles. The variation of rotor angle difference under different initial conditions is shown in Figure 14.

Table 2. BTBS results of the two machines with different initial rotor angles.

Initial Rotor Angel Difference (°)	Start Time of Speed Rise (s)	Rotor Angle Difference at Steady State (°)	Description of BTBS
0	3	17.66	Successful start; Slight oscillation
−90	8	19.24	Successful start; Slight oscillation
−180	10	20.89	Successful start; Moderate oscillation
−270	10	21.19	Successful start; Moderate oscillation

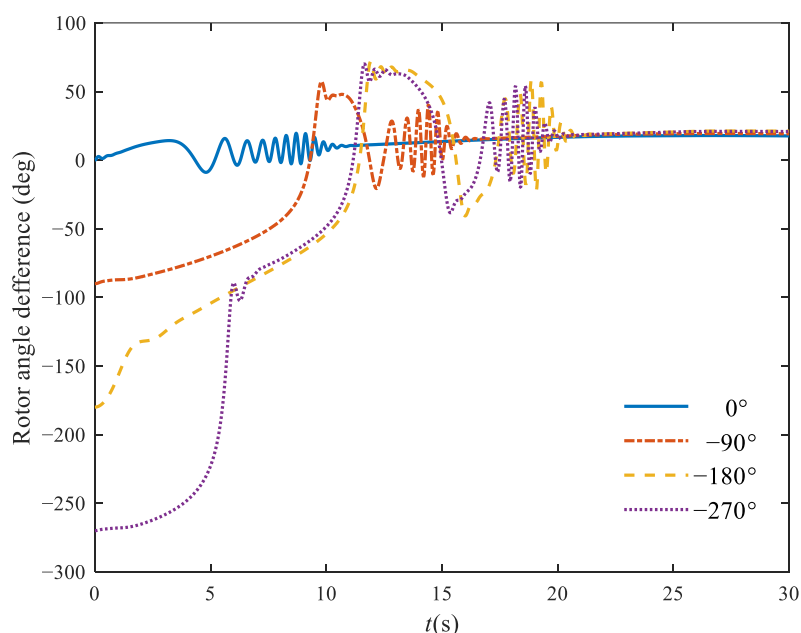


Figure 14. The influence of initial rotor angle differences between two machines.

By observing the simulation results, it can be observed that different initial rotor angles have a certain impact on the startup time of the unit, but have little impact on the target angle difference when the rotor angle difference is stable. With the change of initial rotor angle difference between units, the oscillation in the startup synchronization will change to varying degrees, but it will not affect the successful startup of the unit. Therefore, the influence of the initial difference between rotor positions on BTBS may be ignored.

3.4. Water Head

As an important working condition parameter, the working head is also one of the pivotal influencing factors of the hydraulic machinery transition process, which can be roughly estimated by the water level difference between the upper reservoir and lower reservoir. Here, the changes in water levels above and downstream represent the changes in the working head of the pump turbine, and explore the influence of the working head on BTBS. Therefore, based on the actual unit data of a large PSP in China and the refined model of the PSU, the BTBS process under different working heads is simulated by numerical simulation in this section. The actual data of the unit is as follows: the maximum working head is 217 m, the rated working head is 195 m, and the minimum working head is 178.1 m.

Figure 15 shows the dynamic process trajectory curve of unit flow and unit torque of the tractor under the working head of 200 m, 195 m, 190 m, and 185 m during the BTBS process. For the convenience of comparison, the critical multivalued points of each opening line on the flow characteristic curve and torque characteristic curve are connected to obtain the critical flow line and torque critical line dividing the S-shaped area, as shown in Figure 16. The critical boundary divides the closed area consisting of 0 unit velocity line, 6.9% opening line and 100% opening line into two parts. On the right is the S-shaped area and on the left is the area that can work steadily.

As observed in Figure 15, with the decrease of the working head, the opening of the no-load guide vane of the corresponding back-to-back starting tractor gradually increases. At this time, the unit can easily fall into the S-shaped area at the working point of rated speed. The strong nonlinearity of the pumped storage system in the S-shaped area and the instability of the control system act upon each other, especially when the PSU operates at 185 m head; the flow and torque in the S-shaped characteristic area fall into chaotic operation. This dynamic characteristic will lead the unit speed to swing to and fro, leading to a repeated adjustment of the guide vane opening. If there is no appropriate control strategy, the BTBS process of the unit under a low water head will fail. In summary, under the back-to-back starting condition, the lower the working head of the pump turbine, the more unfavorable it is to the hydraulic mechanical transition process of the unit.

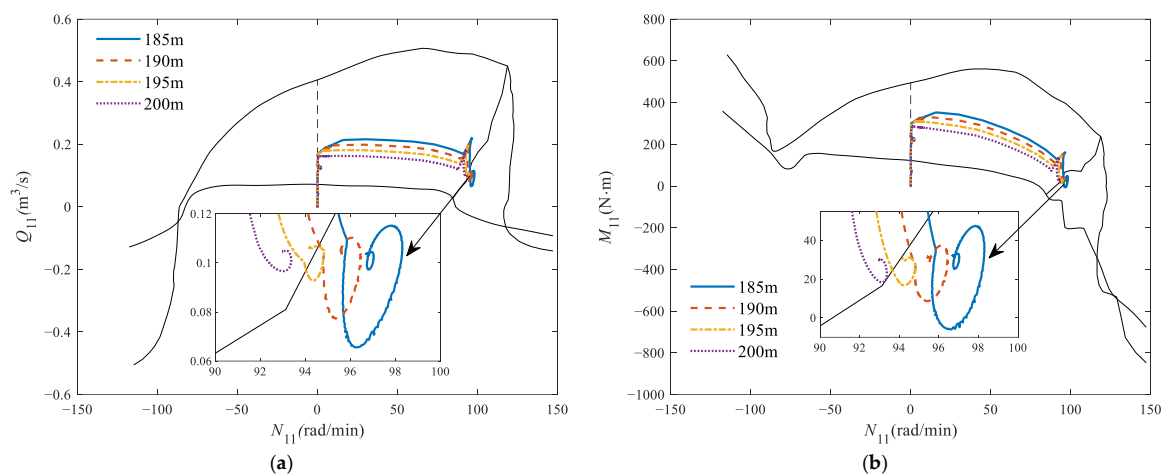


Figure 15. Dynamic process trajectory of moment and torque under different water heads. (a) Dynamic trajectory of flow; (b) Dynamic trajectory of the moment.

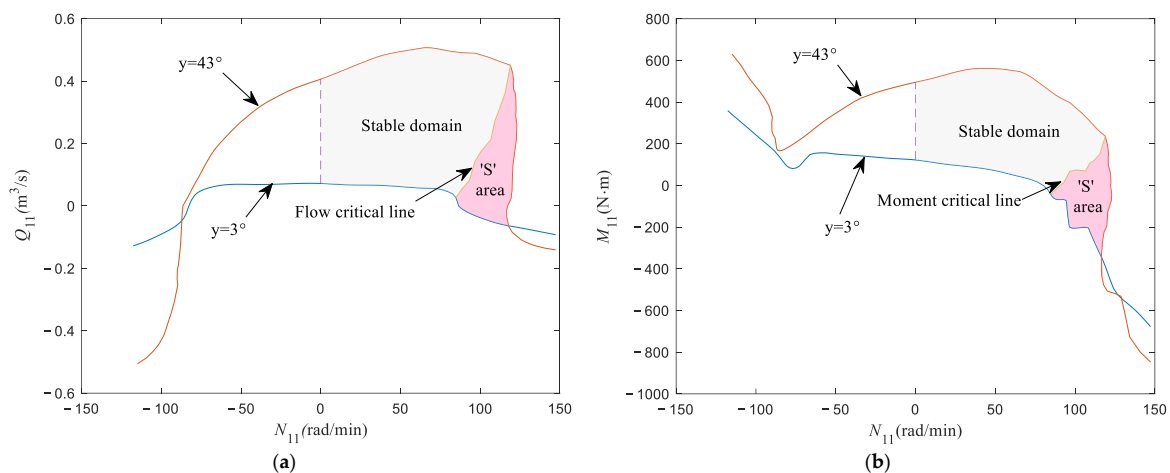


Figure 16. The critical curves of the stable domain and S-shaped region. (a) Flow critical curve; (b) Moment critical curve.

3.5. Control Scheme of the Governor

The BTBS process consists of both open-loop and closed-loop control. The strategy of slowly opening of the guide vane to a certain set point (related to the current water head) is adopted before the rotor speed of the driving machine reaches a certain value ω_s . After accelerating to 0.9, the PID controller is put into operation in closed-loop regulation according to the rated speed, as shown in Figure 17. The rotational speed transition curves of BTBS are plotted at different points of starting time T_s in Figure 18. Generally, the faster the guide vanes are opened, the faster the speeds of the units rise, but this is not absolute. As shown in Figure 18, when the starting time $T_s = 15$ s, the rising speed of the driven machine is faster than the scheme with starting time $T_s = 10$ s.

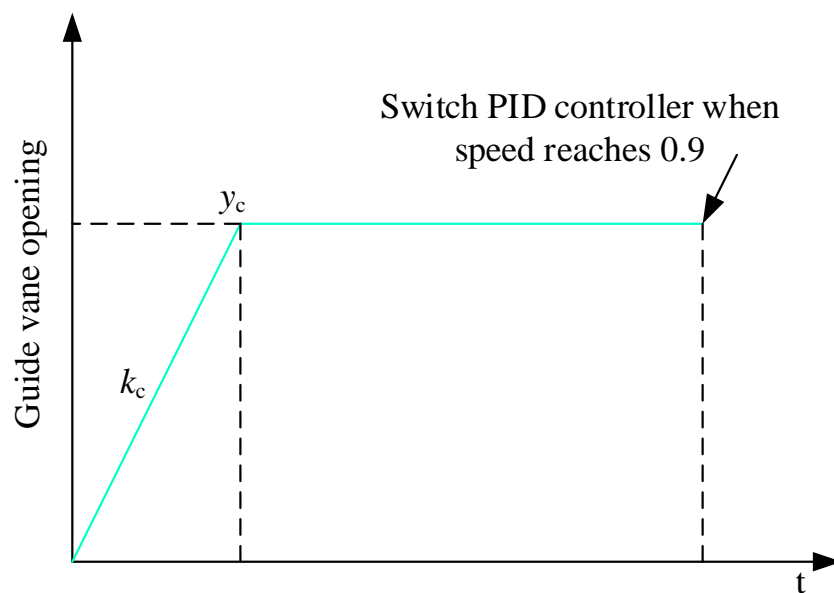


Figure 17. The one-stage direct control law.

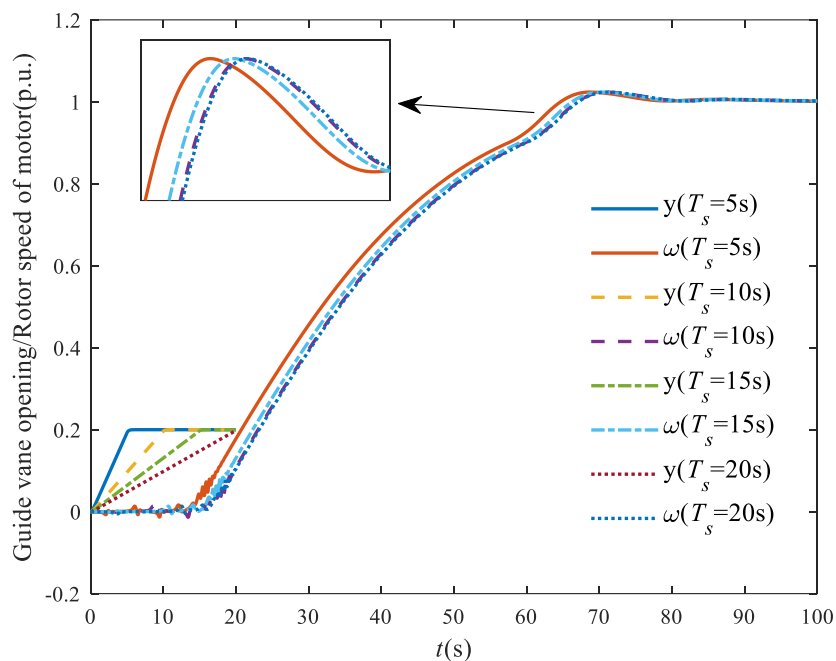


Figure 18. The results of different control schemes.

4. Optimization of BTBS Strategy Based on Multi-Objective Control

It is evident from Section 3 that the excitation current, control way of the excitation system, and control scheme of the governor have a marked impact on the BTBS process. It may even be unsuccessful under the low water head combination of worse control parameters, which is defined as the worst operating condition of BTBS. Therefore, this paper selects the working condition under a low water head as the research object.

The MOPSO algorithm [31,32] is introduced to complete the multi-objective optimization of the BTBS strategy. MOPSO is extensively used in many industries and has outstanding performers in the control optimization of PSU due to its superiority of easy implementation, high precision, and fast convergence [33,34].

4.1. Objective Function

In the BTBS process, the overshoot of rotational speed and the speed stable time can be chosen to respectively represent the stationarity and the rapidity on which we focus. Thus, the overshoot and stable time of rotational speed are included as the evaluation indexes to optimize the BTBS strategy on the basis of multi-objective control. While both evaluation indexes are substitutes, the velocity is more critical, so the speed overshoot of PSU-1 and speed rise time of PSU-2 are chosen as two optimization indexes.

The two objectives are defined as follows:

$$\begin{cases} \min F_1 = \omega_{1\max} - 1 \\ \min F_2 = t_{s2} \end{cases} \quad (10)$$

where $\omega_{1\max}$ is the relative value of the peak speed of driving machine PSU-1, and t_{s2} is the speed stable time of driven machine PSU-2. The description of the objective function is shown in Figure 19.

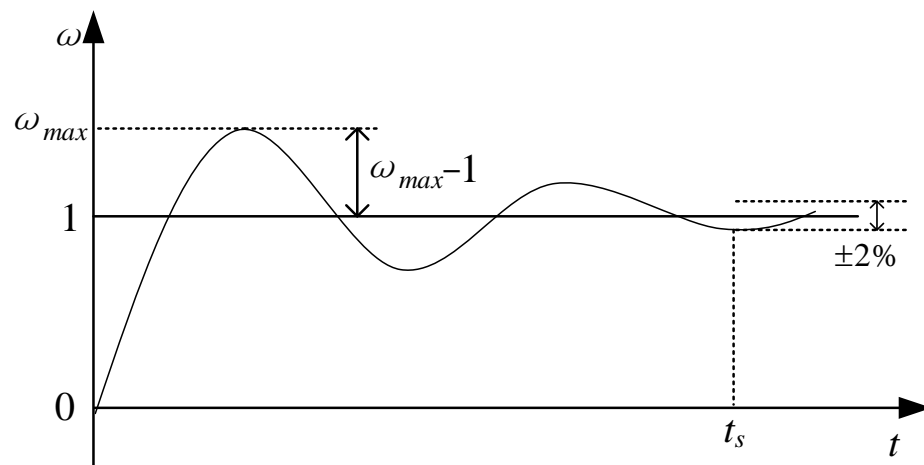


Figure 19. Diagram of speed transition process curve.

4.2. Decision Variables

The decision variable is the parameter of the BTBS strategy. For convenience of analysis, the speed regulation strategy adopts “one-stage guide vane direct opening + PID control”, as shown in Figure 17. This paper studies two excitation strategies: constant excitation current (CEC) and constant excitation voltage (CEV). Their decision variables are summarized as follows:

- Scheme 1: The traditional CEC mode with one-stage DGVC+PID control. In one-stage DGVC, the guide vane of the driving machine is first opened at the rate k_c , and remains unchanged when the guide vane opening reaches y_c . When the speed reaches 90% of

the rated speed, the PID controller will be put into operation. The excitation system of the two units shall first operate with the given excitation current, and switch to the constant terminal voltage mode when the speed reaches 90% of the rated speed. k_c generally takes the maximum rate, which is a known parameter. Therefore, the given excitation current i_g^* , i_m^* , and given opening y_c are selected as the decision variables in the open-loop stage. Parameters of PID controller, K_p , K_i , and K_d , are adopted as the decision variables in the closed-loop stage.

$$X_1 = [i_g^*, i_m^*, y_c, K_p, K_i, K_d] \quad (11)$$

- Scheme 2: The proposed CEV mode with one-stage DGVC+PID control. Similarly, the given excitation voltage V_g^* , V_m^* , given opening y_c , and the three parameters of PID controller, K_p , K_i , and K_d , are chosen as the decision variables.

$$X_2 = [V_g^*, V_m^*, y_c, K_p, K_i, K_d] \quad (12)$$

4.3. Constraint Conditions

There are three types of constraints extracted from engineering limitations according to our experiments in this study.

- (1) Operation Time Constraint

$$0 < t_{s2} < t_{\max} \quad (13)$$

where t_{s2} is the stability time of PSU-2. t_{\max} is the maximum operation time.

- (2) The Boundary of Decision Variables

$$X_i \in [L, U] \quad (14)$$

where X_i is the decision variables of i -th scheme; L and U indicate the lower limits and the upper limits of the boundary.

- (3) Rotor Speed Difference Between Two Machines According to the requirements of the BTBS, the rotational speed difference between the two units shall not exceed a certain limit value; otherwise, it is considered a startup failure:

$$|\omega_1 - \omega_2| \leq \omega_{\max}^d \quad (15)$$

where ω_1 is the rotor speed of the driving machine and ω_2 is the rotor speed of the driven machine. ω_{\max}^d is the maximum allowable rotor speed difference between the two units.

4.4. Optimization Procedures

Based on the nonlinear simulation platform of the PSP system, this study puts forward two multi-objective optimization schemes of BTBS strategy, which are multi-objective constant excitation current (MOCEC) and multi-objective constant excitation voltage (MOCEV). In this subsection, the MOPSO algorithm is introduced to optimize the proposed optimization scheme under the low head condition of BTBS, because once the optimized control schemes can be applied to poor conditions, it is able to adapt to those under normal circumstances. Figure 20 shows the flowchart of the optimization for BTBS with main optimized procedures.

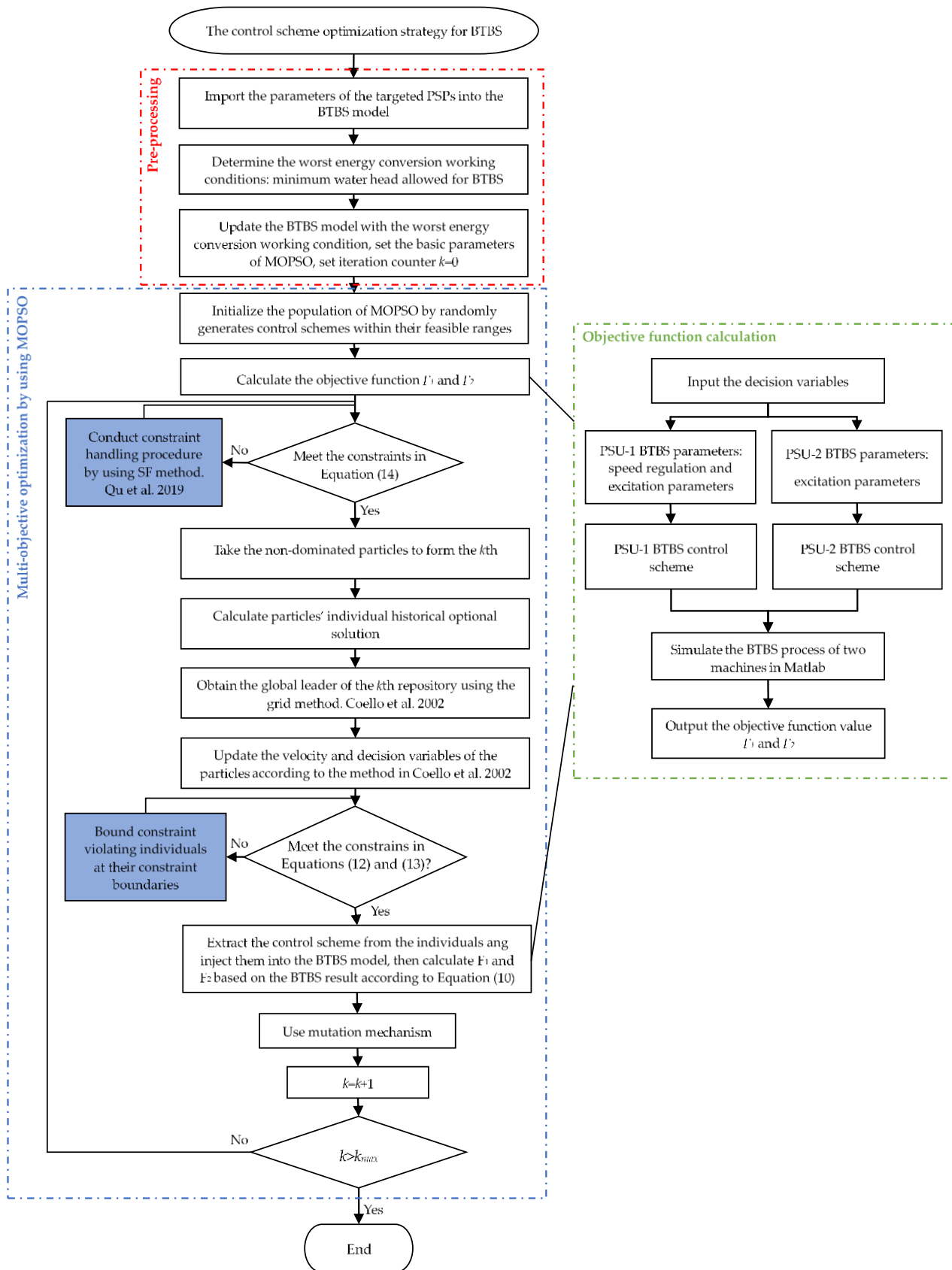


Figure 20. Multi-objective control scheme optimization for BTBS [31,34].

5. Case Study and Analysis

A real PSP in China is taken as the experimental object for the simulation analysis so as to certify the efficacy of the proposed scheme. The layout of the power station is shown in Figure 7. Both units participate in operation; that is, one pipe and two units operate under BTBS conditions. Among them, 1# machine operates as a tractor under the power generation condition of water turbine, and 2# unit operates as a driven machine under the pumping condition of the motor.

5.1. Model Parameters Setting

As shown in Figure 7, the capacities of the two units are the same. The basic parameters of the water diversion system, pump turbine, synchronous machine, governor, and excitation system are the same as those in Section 2.3, as shown in Tables A1–A4. All experiments in this section are carried out under the identical water head; that is, the water level of the upstream reservoir is 291.45 m, and that of the downstream reservoir is 106.11 m. The parameters of the multi-objective optimization algorithm are set as follows: the number of iterations is 200, the population size is 50, the initial value of the inertia weight is 0.5, the size of the external archive is 25, the inertia weight damping is 0.99, and the acceleration constants c_1 and c_2 are both 1.6. According to the analysis of experimental experience and results, the value ranges of decision variables X_1 and X_2 are obtained, as shown in Table 3.

Table 3. Boundaries of decision variables.

Decision Variables	Boundaries	Values					
X_1	L_1	0.1	0.1	0.1	1	0.1	0
	U_1	2.0	2.0	0.4	6	1	6
X_2	L_2	0.1	0.1	0.1	1	0.1	0
	U_2	2.0	2.0	0.4	6	1	6

The multi-objective optimization results named Pareto Set need further ordering to acquire the optimal solution that satisfies the needs of the decision-maker. Therefore, in this section, the multi-objective decision-making method based on relative target proximity is also used to sort the Pareto optimal solution set of MOCEC and MOCEV [35], and the weight information consisting of subjective weight α , objective weight β , and comprehensive weight γ required by the decision-making method are given in Table 4.

Table 4. The weight value of MOCEC and MOCEV schemes.

Schemes	α	β	γ
MOCEC	(0.90, 0.10)	(0.53, 0.47)	(0.91, 0.09)
MOCEV	(0.90, 0.10)	(0.63, 0.36)	(0.94, 0.06)

5.2. Introduction to Comparative Experiments

In order to demonstrate the superiority of the schemes mentioned above, single-objective optimization schemes based on the PSO algorithm are designed as comparative experiments, which are abbreviated as single objective constant excitation current (SOCEC) and single objective constant excitation voltage (SOCEV). The integrated time and absolute error (ITAE) index can be obtained for each unit, as shown in Equations (15) and (16):

$$F_{ITAE1} = \sum_{k=1}^{N_s} t(k) |1 - \omega_1(k)| \quad (16)$$

$$F_{ITAE2} = \sum_{k=1}^{N_s} t(k) |1 - \omega_2(k)| \quad (17)$$

where subscript 1 represents the variable of 1# unit, subscript 2 represents the variable of 2# unit. In order to consider the dynamic process performance indexes of the two units at the same time, the ITAE indexes of the two units are integrated with certain weights w_1 and w_2 as an objective function, as shown in Equation (17):

$$F_{ITAE} = w_1 F_{ITAE1} + w_2 F_{ITAE2} \quad (18)$$

where F_{ITAE} is the objective function of single objective scheme, and w_1 and w_2 are the weight of ITAE index of 1# unit and 2# unit respectively.

5.3. Effectiveness Analysis

For the MOCEC and MOCEV, the optimization result is a set of Pareto optimal solution sets. The particles in the Pareto optimal solution set are non-dominated solutions to each other. The particles in the Pareto optimal solution set are listed in Tables A5 and A6. To make the optimal solution satisfy the needs of the decision-maker, the decision-making method based on relative target proximity is used to sort the particles in the Pareto optimal solution set. The weight value of the decision-making method is shown in Table 4, so the particle ranking is selected as the optimal solution for the multi-objective optimization scheme. Table 5 shows the optimal solutions of the four schemes.

Table 5. Optimal decision variables of four schemes.

Variables \ Schemes	SOCEC	SOCEV	MOCEC	MOCEV
$i_g^*(V_g^*)$	1.2331	0.6599	0.9881	0.6049
$i_m^*(V_m^*)$	0.7422	0.5413	0.6272	0.4437
y_c	0.3985	0.3976	0.1924	0.1929
K_p	3.9083	4.6298	3.5060	3.5941
K_i	0.3630	0.3900	0.1000	0.1000
K_d	0.3190	0.7031	4.9311	5.0779

The optimal decision variables of the four schemes correspond to the four optimal BTBS strategies. The transition process curves of 1# and 2# units under BTBS conditions can be obtained by inputting the four optimal startup strategies into the nonlinear simulation platform of the PSP, as shown in Figure 21. Due to the short adjustment time of field current and rotor angle difference, these two parameters only show the transition process of the first 10 s. The performance indexes of rotor speed are shown in Table 6; $\Delta\omega_{max}$ represents the speed overshoot, t_r represents the speed rise time, and t_s represents the stability time.

In Figure 21a, it can be found that the speed overshoot of single-objective schemes is large, while the speed overshoot of multi-objective schemes is small; the speed fluctuation of multi-objective schemes is also small and the curves are more stable. Figure 21b shows the PSU-2's speed transition processes of the four schemes. It can be observed that the speed curves of single-objective schemes fluctuate more, and the speed curves of the multi-objective schemes are more stable. Figure 21c–h shows the transition curves of other physical quantities. In Figure 21c–d, the field current regulation processes of the four schemes have a certain fluctuation, but the current transition process curve of the MOCEV scheme can reach the steady state fastest and the fluctuation is the smallest. In Figure 21e, the GVO adjustment process of the MOCEV scheme is faster and the oscillation times are the shortest. As seen in Figure 21f, the peak value of rotor angle difference of the four schemes is essentially the same, but the rotor angle fluctuation range of the MOCEV scheme is the smallest. As observed in Figure 21g, the terminal voltage rise processes of the four schemes are slightly different. The terminal voltage rise of the single-objective optimization methods is faster than those of the multi-objective optimization methods, and the impulse generated during voltage control switching of the CEC control scheme is smaller than that of the CEV control scheme. By observing Figure 21h, it can be concluded that during the BTBS under low water head conditions, the multi-objective optimization method can help

the PSU avoid going deep into the S-shape zone, so as to avoid the repeated oscillation of active power and falling into chaos. Therefore, from the analysis of other working indexes of the two units, the multi-objective optimization schemes are better than the single-objective optimization schemes.

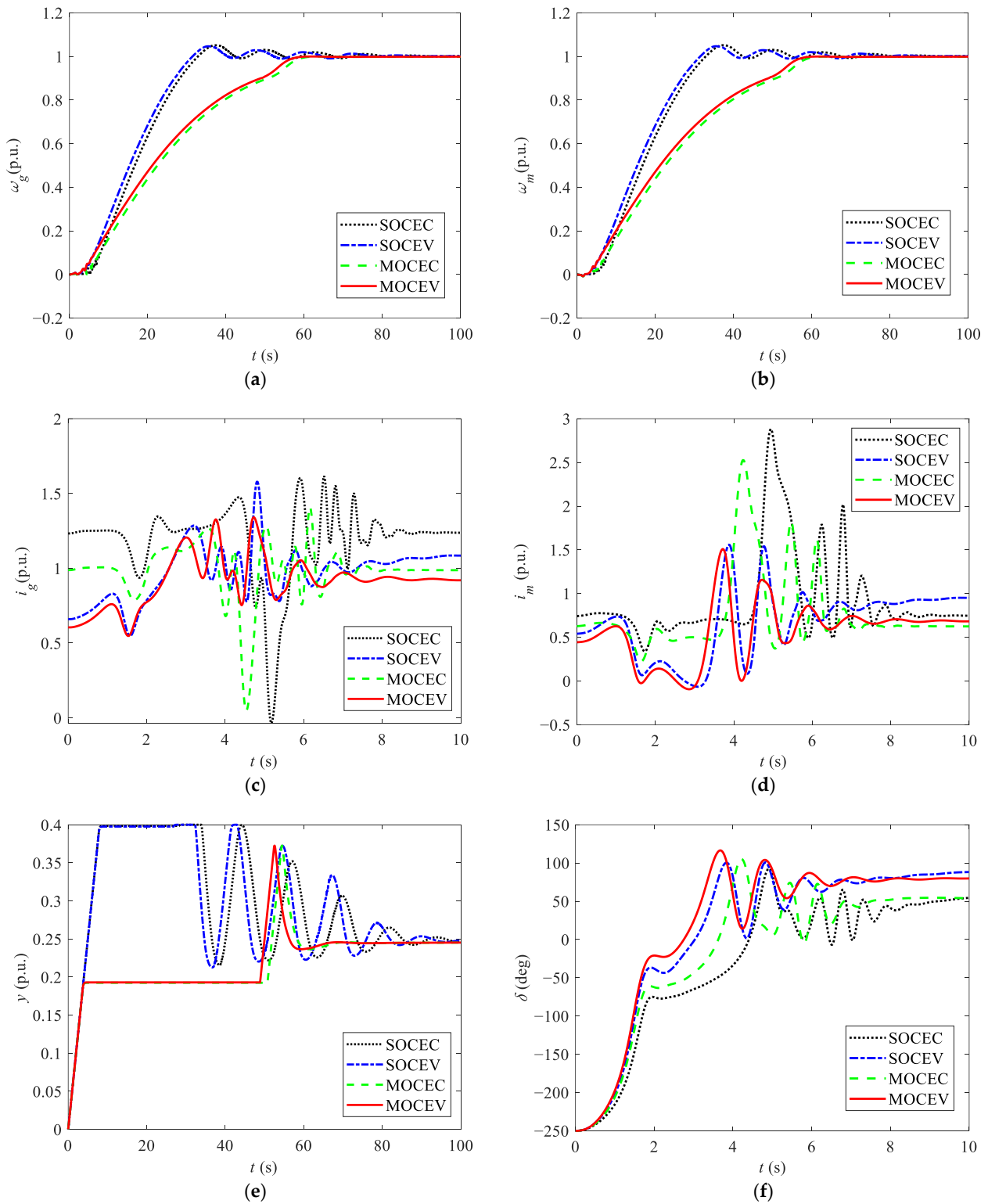


Figure 21. Cont.

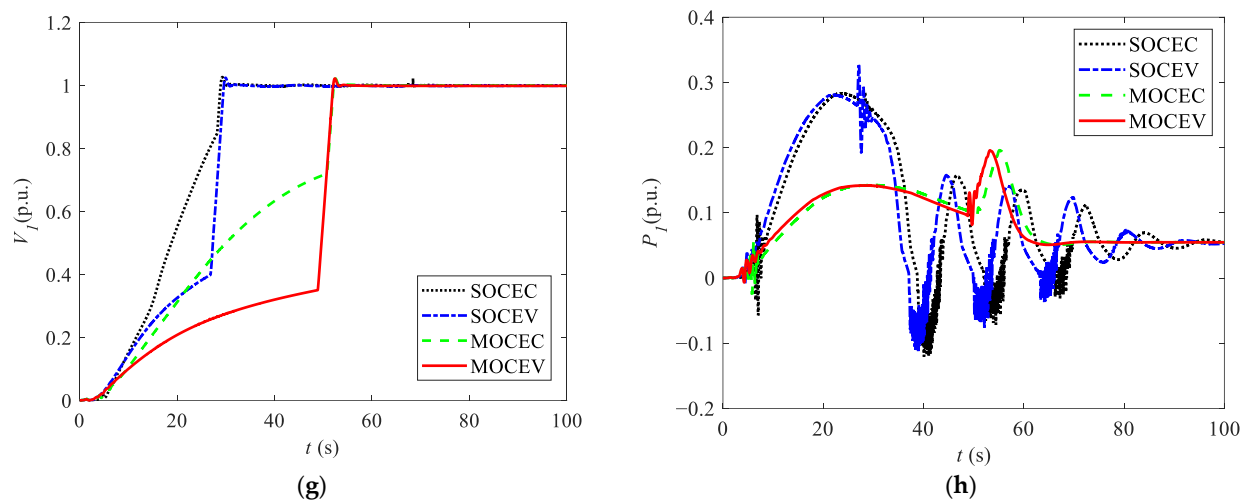


Figure 21. BTBS process of four schemes. (a) Rotor speed of PSU-1; (b) Rotor speed of PSU-2; (c) Field current of PSU-1; (d) Field current of PSU-2; (e) Guide vane opening; (f) Rotor angle difference; (g) Terminal voltage; (h) Active power.

Table 6. Speed performance indexes of four schemes.

Schemes \ Indexes	SOCEC		SOCEV		MOCEC		MOCEV	
	PSU-1	PSU-2	PSU-1	PSU-2	PSU-1	PSU-2	PSU-1	PSU-2
$\Delta\omega_{\max}$	0.0515	0.0518	0.0468	0.0472	2.7796×10^{-5}	4.1466×10^{-5}	8.7973×10^{-6}	2.2633×10^{-5}
t_r (s)	28.20	28.18	26.84	26.82	50.74	50.74	48.86	48.84
t_s (s)	90.68	90.68	99.30	99.30	60.98	60.94	59.00	58.98

For the single-objective schemes, the objective function is the weighted sum of the ITAE indexes of two units. It can be obtained from Table 6 that the speed overshoot of 1# unit is 4.98% and the speed rise time of 2# unit is 26.82 s for SOCEV, which is less than the value of SOCEC, but the speed stable time of 1# and 2# unit of SOCEC are slightly less than the value of SOCEV. For the multi-objective schemes, the objective function is speed overshoot of PSU-1 and speed stable time of PSU-2. The speed overshoot of 1# unit is 0.00088% and the speed stable time of 2# unit is 58.98 s for MOCEV, which is less than the value of MOCEC. Furthermore, comparing different schemes, the speed overshoot of multi-objective optimization schemes is much smaller than those of single-objective optimization schemes, and the speed stable time of multi-objective optimization schemes is also smaller. However, the speed rise time of multi-objective optimization schemes is greater than those of single-objective optimization schemes. In addition, among the four schemes, the speed overshoot of PSU-1 and speed stable time of PSU-2 for MOCEV are the smallest, so it is considered that the optimization effect of the MOCEV scheme is better.

To further reflect the advantages of the multi-objective scheme MOCEV, Figure 22 shows the Pareto fronts of MOCEC and MOCEV schemes.

The Pareto front are even-distributed shown in Figure 22, and the first 25 particles of the MOCEV scheme are non-dominated solutions. If one selects three particles from the far left, middle, and far right for specific analysis, one could simulate their speed transition process curve, as shown in Figure 23. In Figure 23, the speed overshoot of 1# unit of three particles increases in turn, while the speed stable time of 2# unit decreases in turn. Additionally, these three typical particles can help the unit avoid going deep into the S-shaped zone, which ensures the safety and stability of the BTBS process of the PSU under low head conditions. These three particles represent three kinds of particles. Decision-makers may choose one of them as the optimal solution for power plant operation

according to actual needs. There are also 25 particles in front of the MOCEC scheme, and most of them are dominated by the particles at the front of the MOCEV. This phenomenon also shows that the MOCEV scheme is better than the MOCEC.

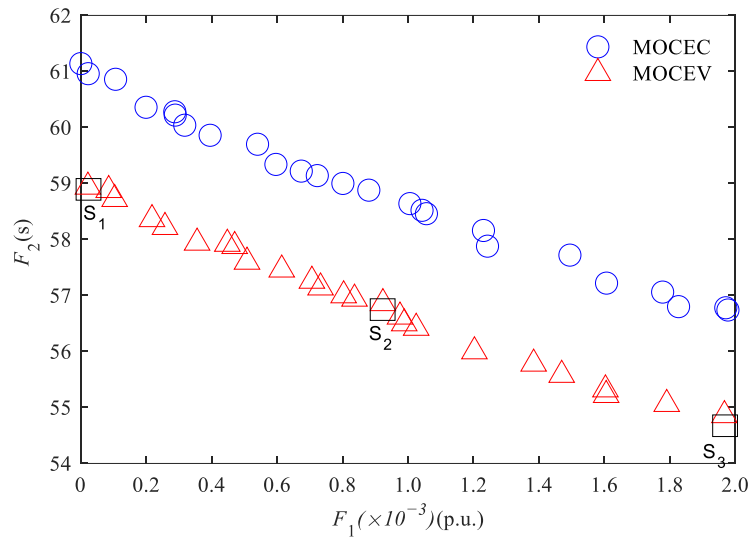


Figure 22. The Pareto fronts obtained by the multi-objective optimization strategy.

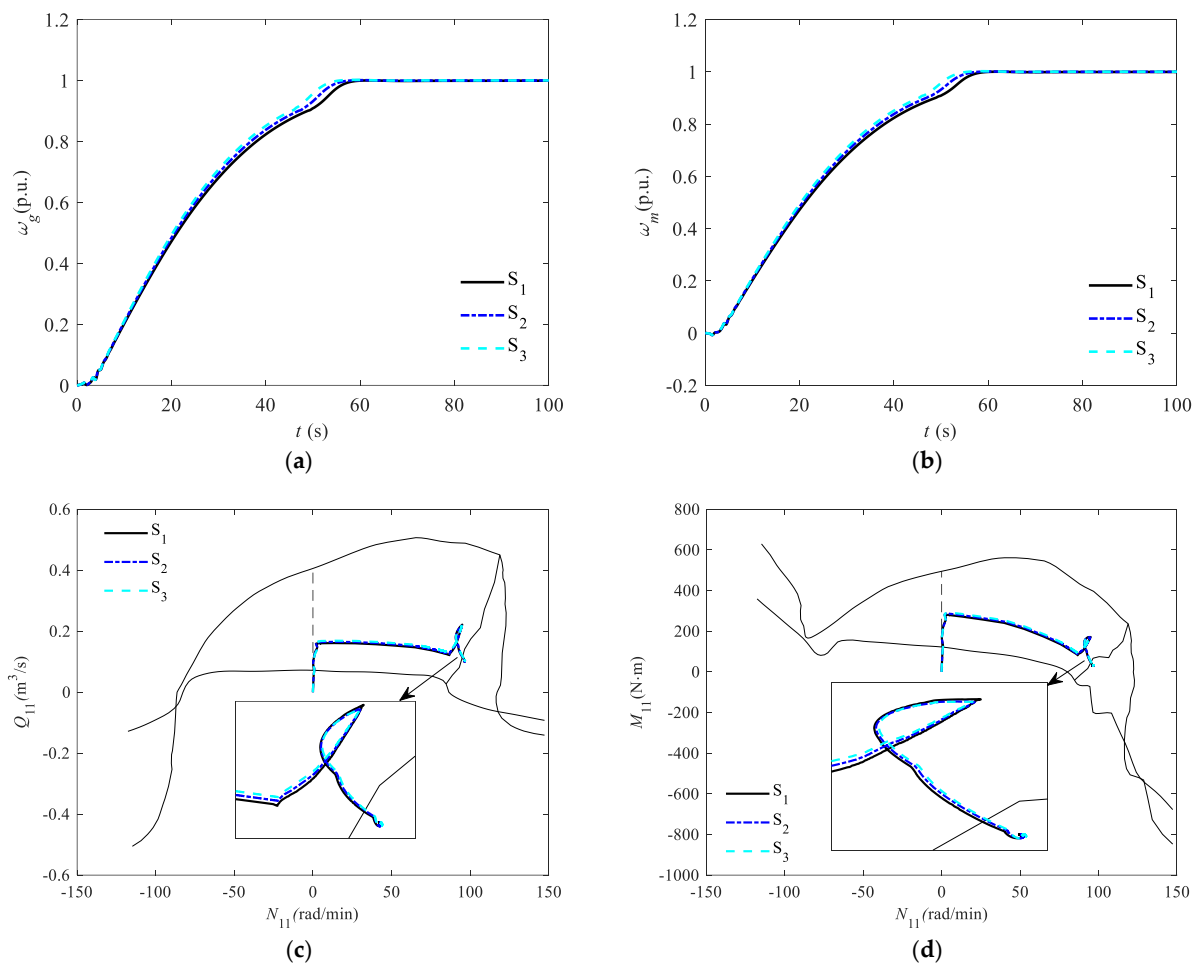


Figure 23. BTBS process of three typical particles. (a) Rotor speed of PSU-1; (b) Rotor speed of PSU-2; (c) Flow trajectory; (d) Moment trajectory.

5.4. Validation of the Proposed Optimization Strategy

This section verifies the effectiveness of the multi-objective optimization method MOCEV for BTBS conditions proposed in this paper under other conditions, and selects different upstream and downstream water levels to form the verification conditions; the corresponding data are listed in Table 7. The parameters of the optimization results in Section 5.4 are respectively substituted into the refined mathematical model of the regulation system of the PSU for the transition process simulation, and the key indicators of the transition process are obtained, as shown in Figure 24.

Table 7. Parameters and MOCEV results under various working conditions of BTBS.

Working Conditions	Water Level		Water Head (m)
	Upstream (m)	Downstream (m)	
N0	291	106	185
N1	295	105	190
N2	298	103	195
N3	303	103	200
N4	303	98	205
N5	308	98	210

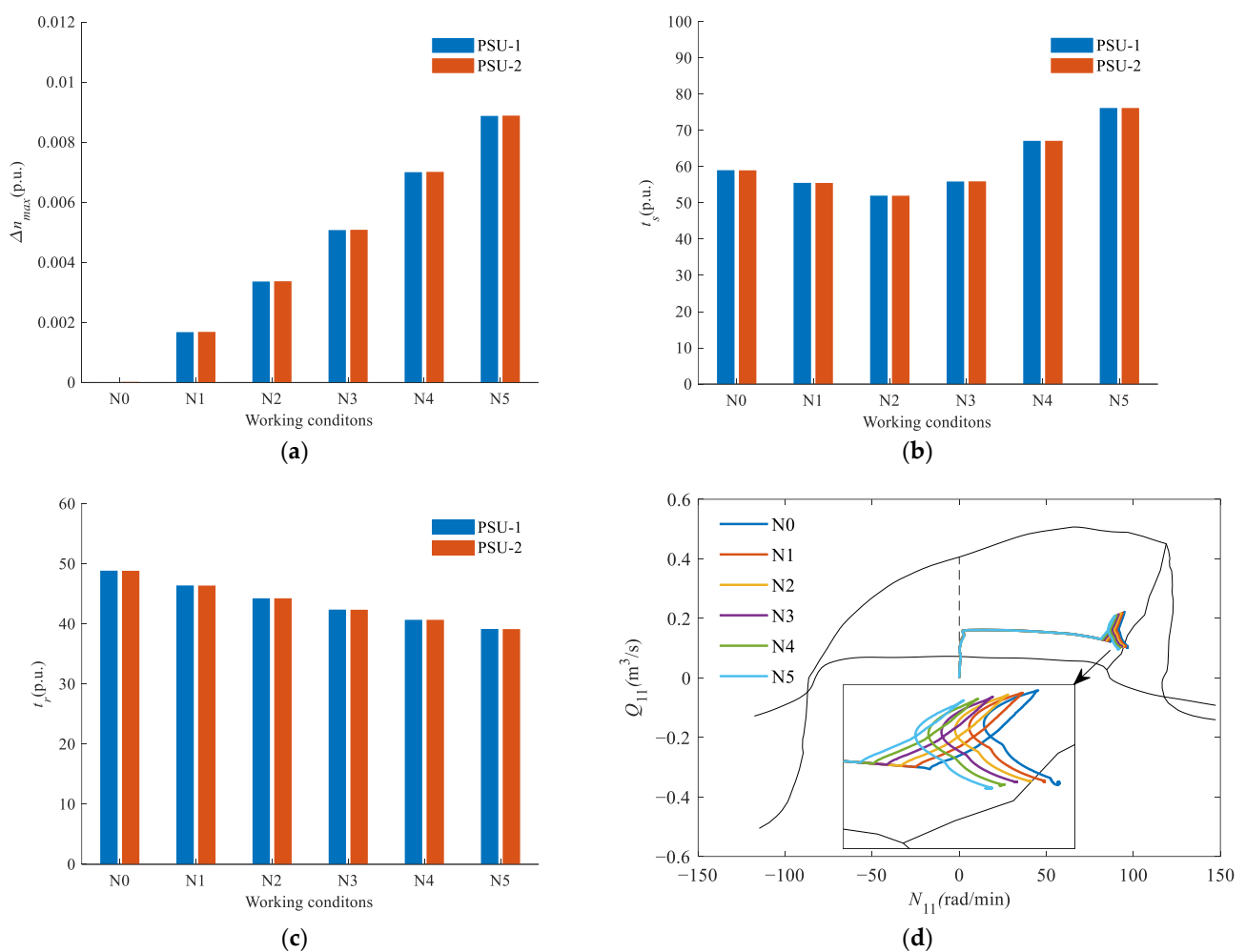


Figure 24. The MOCEV result of the optimal solution under N0–N5. (a) Maximum rotor speed; (b) Speed stable time; (c) Speed rising time; (d) Flow trajectory.

Figure 24a–c shows that, when the multi-objective optimization result is used as the control parameter for BTBS, with the water head increases, the velocity overshoot increases, the velocity stable time decreases first and then increases, and the speed rising time decreases. This is because the no-load GVO under a low water head is larger. When used for open-loop control under other water heads, the speed rise will be faster and the overshoot will be increased. However, in order to ensure that the unit does not fall into the S-shaped area, the integral parameter value under the low head is small, which will lead to a longer time for the speed to reach the steady state under other conditions. Therefore, with the increase of water head, the integral parameters can be appropriately increased to improve the regulation quality under other working conditions. In addition, by observing Figure 24d, it can be concluded that the control parameters optimized under a low water head can prevent the BTBS process of the unit from falling into the S-shaped zone within the full working condition.

6. Conclusions

A refined nonlinear model for BTBS of PSP is developed in this paper, the impacts from the electrical and hydraulic-mechanical subsystem on the operation of PSP during BTBS are investigated subsequently, and a novel MOCEV control strategy is proposed accordingly. The following conclusions are drawn from the simulation results.

1. The given value and control way of excitation current, the control scheme of the governor, and the water head have great influence on the transient process of BTBS. The control scheme of excitation current and guide vane should be selected as the decision variables in the BTBS optimization; the worst BTBS condition can be identified by the lowest water head.
2. The overshoot and stable time of the speed are contradictory. The traditional single-objective optimization scheme merely considers the single objective, which can very easily cause the unit to fall into the S-shaped area, resulting in severe fluctuations in speed and power.
3. Compared with the single-objective, the optimization strategy proposed can considerably improve the speed overshoot and the speed stable time by at least 68.27% and by 3.22% under the worst working condition. The optimization results show that the multi-objective scheme is a better choice than the single-objective scheme.
4. Compared with the MOCEC scheme, when the MOCEV scheme is adopted, the overshoot, rise time, and stable time are improved by 68.35%, 3.7%, and 3.2% in PSU-1, and 45.4%, 3.7%, and 3.2% in PSU-2. Thus, the MOCEV scheme is superior.
5. The proposed MOCEV optimal control scheme can effectively keep away from the S-shaped area and is verified by a real PSU.

Author Contributions: Conceptualization, methodology, software, data curation, writing, original draft preparation, C.F.; writing, editing, corresponding, G.L.; reviewing and editing, supervision, Y.Z.; supervision, D.Z.; visualization, investigation, Z.M. All authors have read and agreed to the published version of the manuscript.

Funding: The Fundamental Research Funds for the Central Universities (B220202005) and the National Natural Science Foundation of China (No. 51979086).

Institutional Review Board Statement: Approval for the study was not required in accordance with local/national legislation.

Informed Consent Statement: Not applicable.

Data Availability Statement: Not applicable.

Conflicts of Interest: The authors declare that they have no known competing financial interest or personal relationships that could have appeared to influence the work reported in this paper.

Nomenclature

Abbreviations

PSP	pumped storage plant
BTBS	back-to-back starting
PSU	pump storage unit
CEV	constant excitation voltage
CEC	constant excitation current
LCP	logarithmic curve projection
MOC	method of characteristics
GVO	gate valve opening
MOCEC	multi-objective CEC
MOCEV	multi-objective CEV
SOCEC	single-objective CEC
SOCEV	single-objective CEV
ITAE	integrated time and absolute error
pu	per-unit value

Symbols

Parameters

A	cross sectional area of pipeline (m^2)
a	wave velocity (m/s)
b_p	permanent difference coefficient (pu)
D	the diameter of the turbine runner (m)
d	pipeline diameter (m)
f	friction coefficient (pu)
g	acceleration of gravity (m/s^2)
K_d	differential gain (pu)
K_e	self-excitation coefficient of exciter (pu)
K_f	damping coefficient (pu)
k_0	forward amplification factor (pu)
K_i	integral gain (pu)
K_p	proportional gain (pu)
R_a	resistance of stator winding (pu)
S_e	exciter saturation factor (pu)
T_a	amplifier time constant (s)
T_b	lead lag time constant (s)
T_c	lead lag time constant (s)
x	distance calculated from upstream (m)
T_d	differential time constant (s)
T_e	exciter time constant (s)
T_f	damping time constant (s)
T_j	mechanical time constant (s)
T_y	main servomotor response time (s)
T_{y1}	assistant servomotor response time (s)
T'_{d0}, T''_{d0}	transient and sub-transient time constants of open-circuit d-axis (s)
T'_{q0}, T''_{q0}	transient and sub-transient time constants of open-circuit q-axis (s)
X_q, X'_q, X''_q	synchronous, transient and sub-transient reactance of q-axis (pu)
X_q, X'_q, X''_q	synchronous, transient and sub-transient reactance of q-axis (pu)

Variables

E'_d, E''_d	the transient and sub-transient internal EMF of d-axis (pu)
E_{fd}	excitation EMF (pu)
E'_q, E''_q	the transient and sub-transient internal EMF of q-axis (pu)
H	piezometric head (m)
H_t	the working head of pump turbine (m)
i_d, i_q	the current of d- and q-axis (pu)
i_{fd}	excitation current (pu)
i_g^*, i_m^*	excitation current setting value of generator and motor (pu)

K_a	amplifier coefficient (pu)
M_e	electromagnetic torque (pu)
M_t	the moment of pump turbine (pu)
M_{11}	unit torque (N/m ³)
N	the rotational speed of the turbine (r/min)
N_{11}	unit speed (m ^{1/2} /s)
N_{11r}	rated unit speed (m ^{1/2} /s)
Q	the water flow rate (m ³ /s)
Q_t	the flow of pump turbine (m ³ /s)
Q_{11}	unit flow (m ^{1/2} /s)
Q_{11r}	rated unit flow (m ^{1/2} /s)
u	controller output signal (pu)
V_g^*, V_m^*	excitation voltage setting value of generator and motor (pu)
v_d, v_q	d- and q-axis component of the voltage (pu)
Y	guide vane opening (deg)
y	main servomotor output signal (pu)
ω, ω^*	relative and given value angular shaft velocity (m)
φ_d, φ_q	the internal EMF of d- and q-axis (pu)
δ	rotor angle (rad)

Appendix A

Table A1. PSP design parameters.

Parameters	Values	Parameters	Values
Rated speed (r/min)	250	Rated capacity (MVA)	334
Rated water-head (m)	195	Rated voltage (kV)	15.75
Rated water flow (m ³ /s)	176.1	Rated current (A)	12,244
Power rating (MW)	306	Rated frequency (Hz)	50
Turbine runner diameter (m)	5.26	Power factor	0.90
100% guide-vane opening (°)	43.01	Moment of inertia (ton/m ²)	19,300

Table A2. Basic parameters of equivalent pipeline of diversion system.

Number	Length (m)	Diameter (m)	Wave Velocity (m/s)	Roughness
L_1	1113.94	9.21	1100	0.014
L_2	206.71	8.97	1120	0.014
L_3	250.77	4.77	1204	0.011
L_4	173.52	6.90	1161	0.010
L_5	260.30	4.80	1204	0.011
L_6	173.52	6.89	1160	0.012
L_7	295.27	10.82	1050	0.014

Table A3. Basic parameters of surge chamber.

Sectional Area of the Impedance Hole (m ²)	Inflow Loss Coefficient	Outflow Loss Coefficient	Sectional Area (m ²)	Altitude (m)
19.63	0.0009217	0.0006767	19.63	231.70~268.30
			380.13	268.30~310.00
			530.93	310.00~320.00

Table A4. Basic parameters of each module of the regulation system model of pumped storage unit.

Excitation System			Synchronous Machine		
T_a	0.001	R_a	0.00125	X''_d	0.2
T_b	0	X_d	1.015	X''_q	0.195
T_c	0	X_q	0.627	T'_{d0}	12.6
T_e	0	X'_d	0.253	T''_{d0}	0.189
T_f	0.1	T_j	10.8	T''_{q0}	0.519
K_a	300	Speed Regulation System			
K_e	1	b_p	0.01	k_0	1
K_f	0.001	T_{y1}	0.02	T_y	0.2

Table A5. The detailed parameters corresponding to the Pareto front solutions of constant excitation current.

Solutions	F_1	$F_2(s)$	i_g^*	i_m^*	y_c	K_p	K_i	K_d
1	0.0000	61.1400	0.9805	0.6135	0.1923	3.4725	0.1000	5.1410
2	0.0000	60.9600	0.9881	0.6272	0.1924	3.5060	0.1000	4.9311
3	0.0001	60.8600	1.0098	0.6266	0.1932	3.4515	0.1000	5.0734
4	0.0002	60.3600	1.0188	0.5930	0.1938	3.6432	0.1000	5.2704
5	0.0003	60.2800	1.0329	0.6127	0.1942	3.5734	0.1000	5.1753
6	0.0003	60.2200	1.0125	0.6208	0.1945	3.5620	0.1000	5.3608
7	0.0003	60.0400	0.9989	0.6175	0.1944	3.5887	0.1000	5.1362
8	0.0004	59.8600	1.0071	0.5973	0.1949	3.5649	0.1000	5.1444
9	0.0005	59.7000	1.0080	0.6061	0.1954	3.3926	0.1000	4.9045
10	0.0006	59.3400	0.9943	0.6156	0.1964	3.5366	0.1000	5.3577
11	0.0007	59.2200	0.9977	0.6136	0.1962	3.4684	0.1000	4.9254
12	0.0007	59.1400	0.9970	0.6167	0.1970	3.4364	0.1000	5.1984
13	0.0008	59.0000	1.0160	0.6366	0.1971	3.5003	0.1000	5.0073
14	0.0009	58.8800	1.0035	0.6084	0.1968	3.3919	0.1000	4.6497
15	0.0010	58.6400	1.0143	0.6353	0.1984	3.3848	0.1000	5.1553
16	0.0010	58.5200	1.0118	0.6244	0.1980	3.3945	0.1000	4.7860
17	0.0011	58.4600	1.0115	0.6289	0.1988	3.3993	0.1000	5.1672
18	0.0012	58.1600	1.0112	0.6271	0.1997	3.3300	0.1000	5.1576
19	0.0012	57.8800	1.0027	0.6149	0.1999	3.4411	0.1000	5.2033
20	0.0015	57.7200	1.0255	0.6064	0.2001	3.2400	0.1000	4.5951
21	0.0016	57.2200	0.9945	0.6315	0.2014	3.3322	0.1000	4.9067
22	0.0018	57.0600	1.0057	0.6203	0.2022	3.2075	0.1000	4.8830
23	0.0018	56.8000	1.0073	0.6276	0.2028	3.3360	0.1000	5.0474
24	0.0020	56.7800	0.9945	0.6364	0.2038	3.3257	0.1000	5.1467
25	0.0020	56.7400	1.0045	0.6287	0.2029	3.1622	0.1000	4.6525

Table A6. The detailed parameters corresponding to the Pareto front solutions of constant excitation voltage.

Solutions	F_1	F_2 (s)	V_g^*	V_m^*	y_c	K_p	K_i	K_d
1	0.0000	58.9400	0.6049	0.4437	0.1929	3.5941	0.1000	5.0779
2	0.0001	58.8800	0.5815	0.4172	0.1928	3.4206	0.1000	4.6254
3	0.0001	58.7200	0.5967	0.4302	0.1940	3.5515	0.1000	5.3448
4	0.0002	58.3600	0.6055	0.4150	0.1949	3.6035	0.1000	5.4766
5	0.0003	58.2200	0.5762	0.4380	0.1946	3.5755	0.1000	5.1809
6	0.0004	57.9400	0.5310	0.4862	0.1955	3.6367	0.1000	5.3869
7	0.0004	57.9200	0.5631	0.4490	0.1956	3.3992	0.1000	4.9775
8	0.0005	57.8800	0.5369	0.4775	0.1963	3.4578	0.1000	5.4568
9	0.0005	57.6000	0.5851	0.4409	0.1962	3.5772	0.1000	5.2510
10	0.0006	57.4600	0.5933	0.4596	0.1962	3.5212	0.1000	4.9430
11	0.0007	57.2600	0.6137	0.4421	0.1975	3.5201	0.1000	5.4057
12	0.0007	57.1400	0.5369	0.4708	0.1974	3.4673	0.1000	5.1295
13	0.0008	57.0000	0.5759	0.4408	0.1976	3.4549	0.1000	5.0178
14	0.0008	56.9400	0.5776	0.4511	0.1979	3.4562	0.1000	5.1085
15	0.0009	56.8600	0.5853	0.4415	0.1986	3.3694	0.1000	5.2359
16	0.0010	56.6200	0.5782	0.5092	0.1990	3.5058	0.1000	5.3278
17	0.0010	56.5000	0.5681	0.4310	0.1991	3.4715	0.1000	5.2946
18	0.0010	56.4200	0.5768	0.4593	0.1992	3.5151	0.1000	5.2587
19	0.0012	56.0000	0.5805	0.4346	0.2003	3.4980	0.1000	5.2770
20	0.0014	55.7800	0.5440	0.4646	0.2010	3.3650	0.1000	5.1138
21	0.0015	55.5800	0.5772	0.4403	0.2013	3.3715	0.1000	5.0147
22	0.0016	55.3200	0.5720	0.4422	0.2023	3.3496	0.1000	5.1389
23	0.0016	55.2200	0.5543	0.4567	0.2024	3.3941	0.1000	5.1392
24	0.0018	55.0600	0.5587	0.4434	0.2027	3.2578	0.1000	4.8341
25	0.0020	54.8600	0.5710	0.4508	0.2037	3.1818	0.1000	4.8972

References

- Zhang, Y.; Zang, W.; Zheng, J.; Cappiotti, L.; Zhang, J.; Zheng, Y.; Fernandez-Rodriguez, E. The influence of waves propagating with the current on the wake of a tidal stream turbine. *Appl. Energy* **2021**, *290*, 116729. [\[CrossRef\]](#)
- Zhang, Y.; Zhang, Z.; Zheng, J.; Zhang, J.; Zheng, Y.; Zang, W.; Lin, X.; Fernandez-Rodriguez, E. Experimental investigation into effects of boundary proximity and blockage on horizontal-axis tidal turbine wake. *Ocean Eng.* **2021**, *225*, 108829. [\[CrossRef\]](#)
- Zhang, Y.; Zhang, J.; Lin, X.; Wang, R.; Zhang, C.; Zhao, J. Experimental investigation into downstream field of a horizontal axis tidal stream turbine supported by a mono pile. *Appl. Ocean Res.* **2020**, *101*, 102257. [\[CrossRef\]](#)
- Zheng, Y.; Chen, Q.; Yan, D.; Liu, W. A two-stage numerical simulation framework for pumped-storage energy system. *Energy Convers Manag.* **2020**, *210*, 112676. [\[CrossRef\]](#)
- Zheng, Y.; Chen, Q.; Yan, D.; Zhang, H. Equivalent circuit modelling of large hydropower plants with complex tailrace system for ultra-low frequency oscillation analysis. *Appl. Math. Model.* **2021**, *103*, 176–194. [\[CrossRef\]](#)
- Feng, C.; Li, C.; Chang, L.; Ding, T.; Mai, Z. Advantage analysis of variable-speed pumped storage units in renewable energy power grid: Mechanism of avoiding S-shaped region. *Int. J. Electr. Power Energy Syst.* **2020**, *120*, 105976. [\[CrossRef\]](#)
- Zeng, W.; Yang, J.; Hu, J. Pumped storage system model and experimental investigations on S-induced issues during transients. *Mech. Syst. Signal Process.* **2017**, *90*, 350–364. [\[CrossRef\]](#)
- Wang, X.; Na, R. Simulation of asynchronous starting process of synchronous motors based on Matlab/Simulink. In Proceedings of the Sixth International Conference on Electrical Machines and Systems, ICEMS 2003 IEEE, Beijing, China, 9–11 November 2003; Volume 2, pp. 684–687.
- Wang, F.; Jiang, J. A novel static frequency converter based on multilevel cascaded H-bridge used for the startup of synchronous motor in pumped-storage power station. *Energy Convers Manag.* **2011**, *52*, 2085–2091. [\[CrossRef\]](#)
- Magsaysay, G.; Schuette, T.; Fostiak, R.J. Use of a static frequency converter for rapid load response in pumped-storage plants. *IEEE Trans. Energy Convers.* **1995**, *10*, 694–699. [\[CrossRef\]](#)
- Li, B.; Duan, Z.; Wu, J. Short-circuit analysis of pumped storage unit during back-to-back starting. *IET Renew. Power Gener.* **2015**, *9*, 99–108. [\[CrossRef\]](#)
- Konidaris, D.N. Investigation of back-to-back starting of pumped storage hydraulic generating units. *IEEE Trans. Energy Convers.* **2002**, *17*, 273–278. [\[CrossRef\]](#)
- Xu, Y.; Zhou, J.; Xue, X.; Fu, W.; Zhu, W.; Li, C. An adaptively fast fuzzy fractional order PID control for pumped storage hydro unit using improved gravitational search algorithm. *Energy Convers. Manag.* **2016**, *111*, 67–78. [\[CrossRef\]](#)
- Chaudhry, H. *Applied Hydraulic Transients*, 3rd ed.; Springer: Berlin/Heidelberg, Germany, 2014.

15. Osburn, G.D.; Atwater, P.L. Design and testing of a back-to-back starting system for pumped storage hydrogenerators at Mt. Elbert Powerplant. *IEEE Trans. Energy Convers.* **1992**, *7*, 280–288. [[CrossRef](#)]
16. Rajamani, K.; Hariharan, M.V. Synchronous starting of synchronous machine. *Electr. Mach. Power Syst.* **1993**, *21*, 647–661. [[CrossRef](#)]
17. Karmaker, H.; Mi, C. Improving the starting performance of large salient-pole synchronous machines. *IEEE Trans. Magn.* **2004**, *40*, 1920–1928. [[CrossRef](#)]
18. Xiao, S.; Liu, J.; Kang, X. The coordination of Back-to-back starting and protections for pumped storage units. In Proceedings of the Asia-Pacific Power and Energy Engineering Conference, Shanghai, China, 27–29 March 2012; pp. 1–4.
19. Ghazvini, M.; Pourkiaei, S.M.; Pourfayaz, F. Thermo-economic assessment and optimization of actual heat engine performance by implementation of NSGA II. *Renew. Energy Res. Appl.* **2020**, *1*, 235–245.
20. Beiranvand, A.; Ehyaei, M.A.; Ahmadi, A.; Silvaria, J.L. Energy, exergy, and economic analyses and optimization of solar organic Rankine cycle with multi-objective particle swarm algorithm. *Renew. Energy Res. Appl.* **2021**, *2*, 9–23.
21. Sabbagh, O.; Fanaei, M.A.; Arjomand, A.; Ahmadi, M.H. Multi-objective optimization assessment of a new integrated scheme for co-production of natural gas liquids and liquefied natural gas. *Sustain. Energy Technol. Assess.* **2021**, *47*, 101493. [[CrossRef](#)]
22. Pourkiaei, S.M.; Pourfayaz, F.; Mehrpooya, M.; Ahmadi, M.H. Multi-objective optimization of tubular solid oxide fuel cells fed by natural gas: An energetic and exergetic simultaneous optimization. *J. Therm. Anal. Calorim.* **2021**, *145*, 1575–1583. [[CrossRef](#)]
23. Xu, Y.; Zheng, Y.; Du, Y.; Yang, W.; Peng, X.; Li, C. Adaptive condition predictive-fuzzy PID optimal control of start-up process for pumped storage unit at low head area. *Energy Convers. Manag.* **2018**, *177*, 592–604. [[CrossRef](#)]
24. Wylie, E.B.; Streeter, V.L.; Suo, L. *Fluid transients in systems*; Prentice Hall: Englewood Cliffs, NJ, USA, 1993.
25. Chaudhry, M.H. Characteristics and Finite-Difference Methods. In *Applied Hydraulic Transients*; Springer: New York, NY, USA, 2014; pp. 65–113.
26. Lai, X.; Li, C.; Zhou, J.; Zhang, N. Multi-objective optimization of the closure law of guide vanes for pumped storage units. *Renew. Energy* **2019**, *139*, 302–312. [[CrossRef](#)]
27. Machowski, J.; Lubosny, Z.; Bialek, J.W. *Power System Dynamics: Stability and Control*; John Wiley & Sons: Hoboken, NJ, USA, 2020.
28. Grigsby, L.L. *Power System Stability and Control*; CRC press: Boca Raton, FL, USA, 2007.
29. Yang, W.; Norrlund, P.; Bladh, J.; Yang, J.; Lundin, U. Hydraulic damping mechanism of low frequency oscillations in power systems: Quantitative analysis using a nonlinear model of hydropower plants. *Appl. Energy.* **2018**, *212*, 1138–1152. [[CrossRef](#)]
30. Zhao, L.; Gong, Z.S. Application of ABB F series excitation regulator in synchronous motor. *Electr. World* **2006**, *47*, 1–5. (In Chinese)
31. Coello, C.A.C.; Lechuga, M.S. MOPSO: A proposal for multiple objective particle swarm optimization. In Proceedings of the 2002 Congress on Evolutionary Computation, Honolulu, HI, USA, 12–17 May 2002; Volume 2, pp. 1051–1056.
32. Sheikholeslami, F.; Navimipour, N.J. Service allocation in the cloud environments using multi-objective particle swarm optimization algorithm based on crowding distance. *Swarm Evol. Comput.* **2017**, *35*, 53–64. [[CrossRef](#)]
33. Hou, J.; Li, C.; Guo, W.; Fu, W. Optimal successive start-up strategy of two hydraulic coupling pumped storage units based on multi-objective control. *Int. J. Electr. Power Energy Syst.* **2019**, *111*, 398–410. [[CrossRef](#)]
34. Qu, B.Y.; Suganthan, P.N. Constrained multi-objective optimization algorithm with an ensemble of constraint handling methods. *Eng. Optim.* **2011**, *43*, 403–416. [[CrossRef](#)]
35. Song, H.Z. A method based on objective adjacent scale for multi-objective decision-making and its application. *Math. Pract. Theory* **2004**, *5*, 30–36.